# ARTseq-FISH reveals position-dependent differences in gene expression of micropatterned mESCs

**Xinyu Hu[1,2], Bob van Sluijs[1,2], Óscar García-Blay[1], Yury Stepanov[1], Koen Rietrae[1], Wilhelm T.S. Huck[1,*], Maike M. K. Hansen[1,*].**

**Affiliations:**
[1]Institute for Molecules and Materials, Radboud University, Heyendaalseweg 135, 6525 AJ Nijmegen, the Netherlands.
[2]These authors contributed equally to this work: Xinyu Hu, Bob van Sluijs.
*Correspondence to: w.huck@science.ru.nl (W.T.S.H); maike.hansen@ru.nl (M.M.K.H)

**Abstract:** Differences in gene-expression profiles between individual cells can give rise to distinct cell fate decisions. Yet how localisation on a micropattern impacts initial changes in mRNA, protein, and phosphoprotein abundance remains unclear. To identify the effect of cellular position on gene expression, we developed a scalable antibody and mRNA targeting sequential fluorescence *in situ* hybridization (ARTseq-FISH) method capable of simultaneously profiling mRNAs, proteins, and phosphoproteins in single cells. We studied 67 (phospho-)protein and mRNA targets in individual mouse embryonic stem cells (mESCs) cultured on circular micropatterns. ARTseq-FISH reveals relative changes in both abundance and localization of mRNAs and (phospho-)proteins during the first 48 hours of exit from pluripotency. We confirm these changes by conventional immunofluorescence and time-lapse microscopy. Chemical labelling, immunofluorescence, and single-cell time-lapse microscopy further show that cells closer to the edge of the micropattern exhibit increased proliferation compared to cells at the centre. Together these data suggest that while gene expression is still highly heterogeneous position-dependent differences in mRNA and protein levels emerge as early as 12 hours after LIF withdrawal.

## Introduction

A complex interplay of signalling pathways and transcriptional networks guides morphological transformations during mammalian development[1-3]. During early development the balance between key signalling pathways defines the cellular choice between differentiation and self-renewal[4-6]. Therefore, early changes in mRNA and protein expression levels can influence cell fate decisions[7-9]. Micropatterning has proven to be a powerful tool in unveiling position-dependent differentiation that recapitulates the spatial patterning of germ layers observed in early embryonic development[10-17]. Measuring mRNA and protein levels as mouse embryonic stem cells (mESCs) exit pluripotency will offer insights into how micropattern positioning affects early gene expression changes. This requires a scalable image-based approach capable of simultaneously detecting and quantifying mRNAs and proteins with a high spatial resolution across large areas.

Recently, next generation sequencing (NGS)-based spatial-omics methods have greatly increased the multiplexing capacities of RNA or protein detection, albeit with low efficiency due to *in situ* reverse transcription and limited resolution of the beads used to capture targets[18-22]. Techniques that resolve the resolution issue, predominantly for RNA, are image-based spatial-omics methods. Image-based transcriptomic methods have greatly expanded the number of transcripts that can be resolved, using sequential fluorescence *in situ* hybridization (FISH)[23-27] and barcoding approaches[24-27]. These methods have been combined with immunofluorescence (IF), but multiplexed protein detection remains a challenge[28]. For example, targeting and visualizing RNAs and proteins often require separate sequential experimental and imaging steps, doubling the experimental time[26]. Thus, scaling of these techniques in terms of multiplexing capabilities are bottlenecks, limiting the ability to simultaneously visualize mRNAs and proteins in high throughput[29-32]. Furthermore, the resolution of protein detection is often below the level of RNA detection proving a barrier to quantitative insights into protein location or spatial correlation of RNA and protein abundance[24, 26, 28-32]. Conversely, DNA-barcoding dependent methods (for example, CODEX[33], ImmunoSABER[34] and InSituPlex®[35]) have shown their multiplexing capacity in protein detection, but have thus far not been integrated with RNA detection[36, 37].

Here we develop and validate a multiplexed spatial profiling method: antibody-mRNA targeted sequential FISH (ARTseq-FISH). This method enables simultaneous quantification of mRNA, protein, and phosphoprotein levels in individual mouse embryonic stem cells (mESCs) with high spatial resolution. The gene expression profiles of 67 targets were analysed during the initial 48 hours of differentiation, allowing us to capture relative changes in mRNA and protein abundance as mESCs exit pluripotency. Similar to previous evidence[15, 16], ARTseq-FISH reveals distinct gene-expression profiles in cells located at different positions on the micropattern. Specifically, position-dependent differences in gene expression profiles emerge already during the first 12 hours of Leukemia inhibitory factor (LIF) withdrawal. Finally, we confirm that cells closer to the edge of the micropattern display increased proliferation compared to cells at the centre of the micropattern already during the first 12 hours of LIF withdrawal. In summary, here we describe and validate a method that quantifies relative differences in mRNA and (phospho)protein abundance.

## Results

### ARTseq-FISH enables simultaneous visualization of mRNAs, proteins, and phosphoproteins

The ARTseq-FISH workflow comprises a series of consecutive steps (Fig. 1a and d, Supplementary Notes 1, Supplementary Fig. 1-16). In short, fixed cells are stained with DNA-barcoded antibodies against (phospho-)protein targets of choice (Supplementary Table 1-2). The DNA-barcode of each antibody, known not to influence antibody binding efficeincy[38, 39], contains a 10-nt polyadenylation (poly A) linker and a specific 36-nt sequence that is complementary to a corresponding target-specific single stranded DNA (ssDNA) padlock probes (PLPs). On the other hand, cellular mRNAs are directly targeted by one specific ssDNA PLP with a target sequence of 36-nt (Supplementary Fig. 1a-b), resulting in DNA/RNA hybridization. Therefore, the circularizing of the PLPs that hybridize to either proteins or RNAs require T4 DNA ligase and SplintR ligase respectively[40-42] (Fig.1a, Supplementary Fig. 4-6). Next, rolling circle amplification (RCA) generates rolling circle products (RCPs) that amplify the original (phospho-)protein or mRNA target (Fig. 1a and Supplementary Fig. 8). To decode the original target amplified by the RCPs, we first hybridize target-specific bridge probes (BrPs), which are each recognized by unique combinations of fluorescently labelled readout probes (RoPs) (Fig. 1a, Supplementary Fig.1c-d, Supplementary Fig. 9, and Supplementary Table 1), allowing the detection of individual spots for each mRNA and protein (Fig. 1b-c, Supplementary Fig. 17-18). ARTseq-FISH provides similar relative protein abundance compared to classic immunofluorescence (Supplementary Fig. 19). We determined a detection efficiency of ~47% (for *Nanog* mRNA) by comparing mRNA quantification using ARTseq-FISH with conventional single molecule RNA FISH (smFISH)[27] (Supplementary Fig. 20, Supplementary Table 3). Furthermore, ARTseq-FISH enhances the signal ~4-fold with respect to conventional smFISH (Supplementary Fig. 20c-d), resulting in a higher signal-to-noise ratio. On average, ~0.03-0.5 spots per cell detected as false positives from unspecific PLP (protein detection only), BrP, and RoP hybridization (Supplementary Fig. 3), in particular in the presence of true hybridization signal (Supplementary Fig. 18b). Similar to existing methods, we are unable to quantify the degree of false positives coming from unspecific binding of the antibody or PLP and the target detection efficiency is highly antibody[33, 34] and PLP-dependent[40-43] (Supplementary Fig. 10). Lastly, here we specifically employ one PLP per mRNA target, since we are interested in relative mRNA differences. However, should more rigorous quantification of mRNA be necessary at least 3 PLPs per target are likely required[40-43].

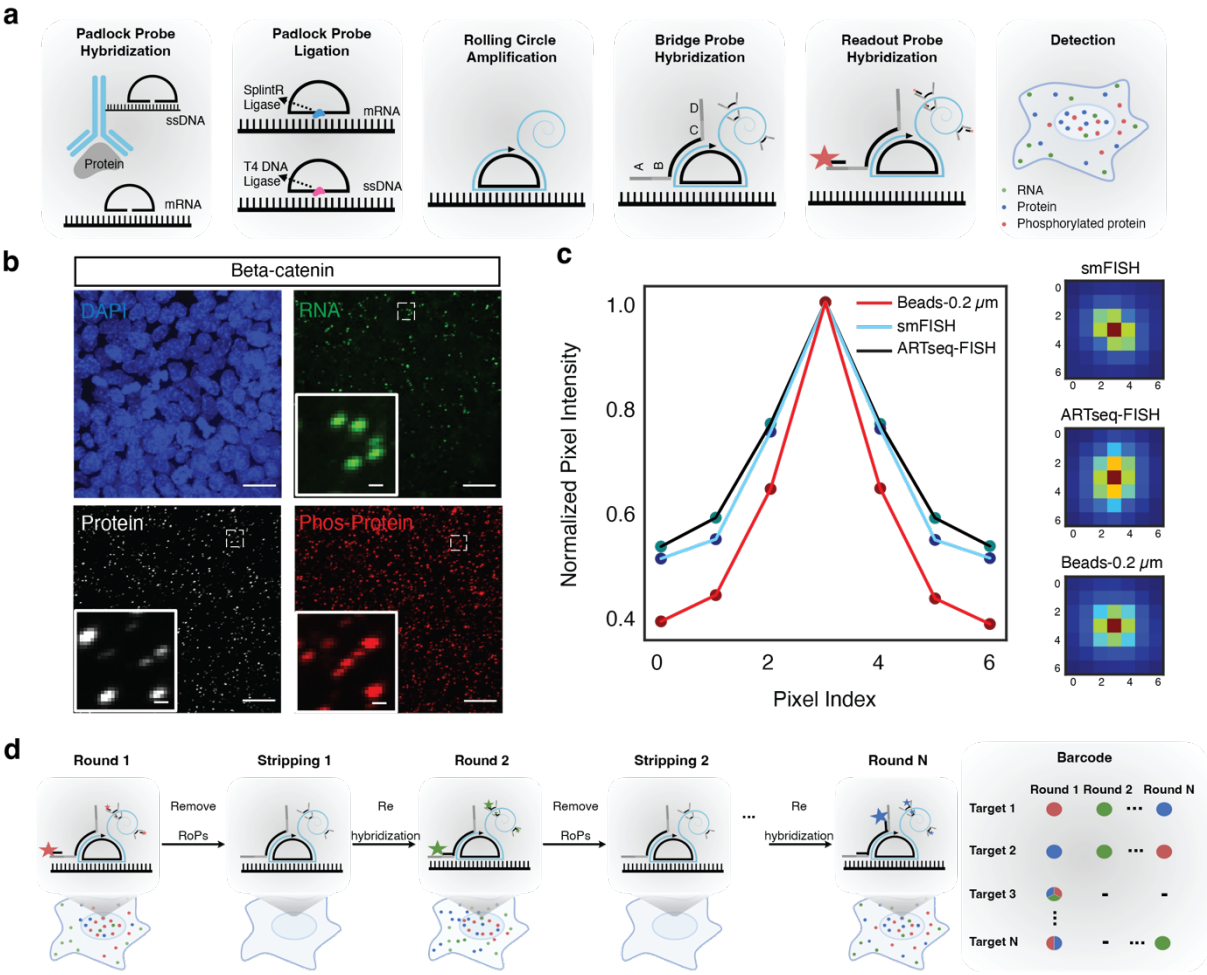


**Fig. 1: Experimental outline of ARTseq-FISH. a,** The experimental workflow of ARTseq-FISH enables detection of different molecular species (mRNA, proteins, and phosphoproteins) simultaneously. Each antibody conjugated to oligonucleotides, targets its associated (phospho-)protein *in situ*. Target-specific PLPs bind to these oligonucleotides as well as cellular mRNA, respectively. Then the PLPs are circularized and amplified into RCPs. A set of target-specific BrPs hybridize to RCPs and then RoPs labelled with fluorophores bind to one of the four flanking sequences on the BrP. **b,** Representative raw data of simultaneously detecting *Beta-catenin* mRNA, protein, and phosphoprotein with same resolution. Scale bar, 20 µm, 1 µm. **c,** The relative mean pixel intensity of the hybridization signal's point spread functions (n = 2000) around the local maxima. Comparison of the average observed signal of ARTseq-FISH to smFISH and a 200 nm fluorescent bead. **d,** The sequential stripping and rehybridization of a new known RoPs allows subsequent decoding of stacked signals.

## Automated analysis and quantification of mRNAs and proteins in single cells

Multiplexed, simultaneous, detection and quantification of mRNAs and (phospho-)proteins over a large area is achieved through serial stripping and rehybridization of RoPs following a predetermined colour barcoding scheme[27] (Fig. 1d, Methods, Supplementary Notes 1-2, Supplementary Fig. 14-16, Supplementary Table 4). The barcode of each target is determined by the presence of a given colour (green, red, or far red) in a sequence of specific hybridization rounds. To correctly decode the detected signal and translate this into mRNA or protein counts for individual cells, we developed an automated image analysis pipeline that returns the abundance of each target per cell.

The pipeline (Fig. 2a, more detailed description in Supplementary Notes 2, SN2 Fig. 1-3, software packages used[44-49]) initiates the analysis by identifying the local maxima per colour channel[50] by denoising and sharpening the image in 6 steps (SN2 Fig. 3-4) and classifying the local maxima as a true hybridization signal. This is done by using a support vector machine

133 (SVM) model trained on data of true point spread functions, which allows for signal
134 deconvolution (SN2 Fig. 5-6). Single cell analysis requires the reconstruction of single cells in
135 3D from a collection of images (Fig. 2a and SN2 Fig. 7-15). However, consistent segmentation
136 is challenging because a segmentation algorithm that maps onto one nucleus might not map
137 onto others (SN2 Fig. 8), or a global image filter that cleanly separates the nuclei in one image
138 might not be optimal for another (SN2 Fig. 10). Therefore, an iterative approach was
139 implemented, repeatedly segmenting nuclei using different global image filters and
140 segmentation parameters[51] (SN2 Fig. 9 and 13). We collected the segmentation labels and used
141 an SVM model to filter out any failed segmentations. The remaining labels were subsequently
142 used to reconstruct the nuclei in 3D by clustering their centroids with a node-based graph (SN2
143 Fig. 14-15). After interpolating any missing nucleus segmentations across the z-axis, we
144 obtained a 3D bounding box. Another SVM model subsequently assessed if this bounding box
145 contains a single nucleus. Before assigning mRNA and protein counts to a cell, we adjusted for
146 any drift, by using the segmented nuclei as unique markers to align the images. Once a global
147 shift was found, we refined the alignment by moving all hybridization signals across a narrow
148 range of shifted pixels until the signals overlapped (SN2 Fig. 16-17). Ultimately, we decoded
149 the overlapping signals and assigned each hybridization signal to a particular protein or mRNA
150 in a specific cell (Fig. 2b, Supplementary Fig. 2, SN2 Fig.18-19). Notably, we assign each
151 target to a specific cell based on the shortest distance to the nucleus. Therefore, although the
152 cellular spot count correlates strongly with the nuclear spot count (SN2 Fig. 23), there is a
153 possibility of incorrect assignments if the distance from the nucleus to the cell membrane varies
154 significantly between neighbouring cells.

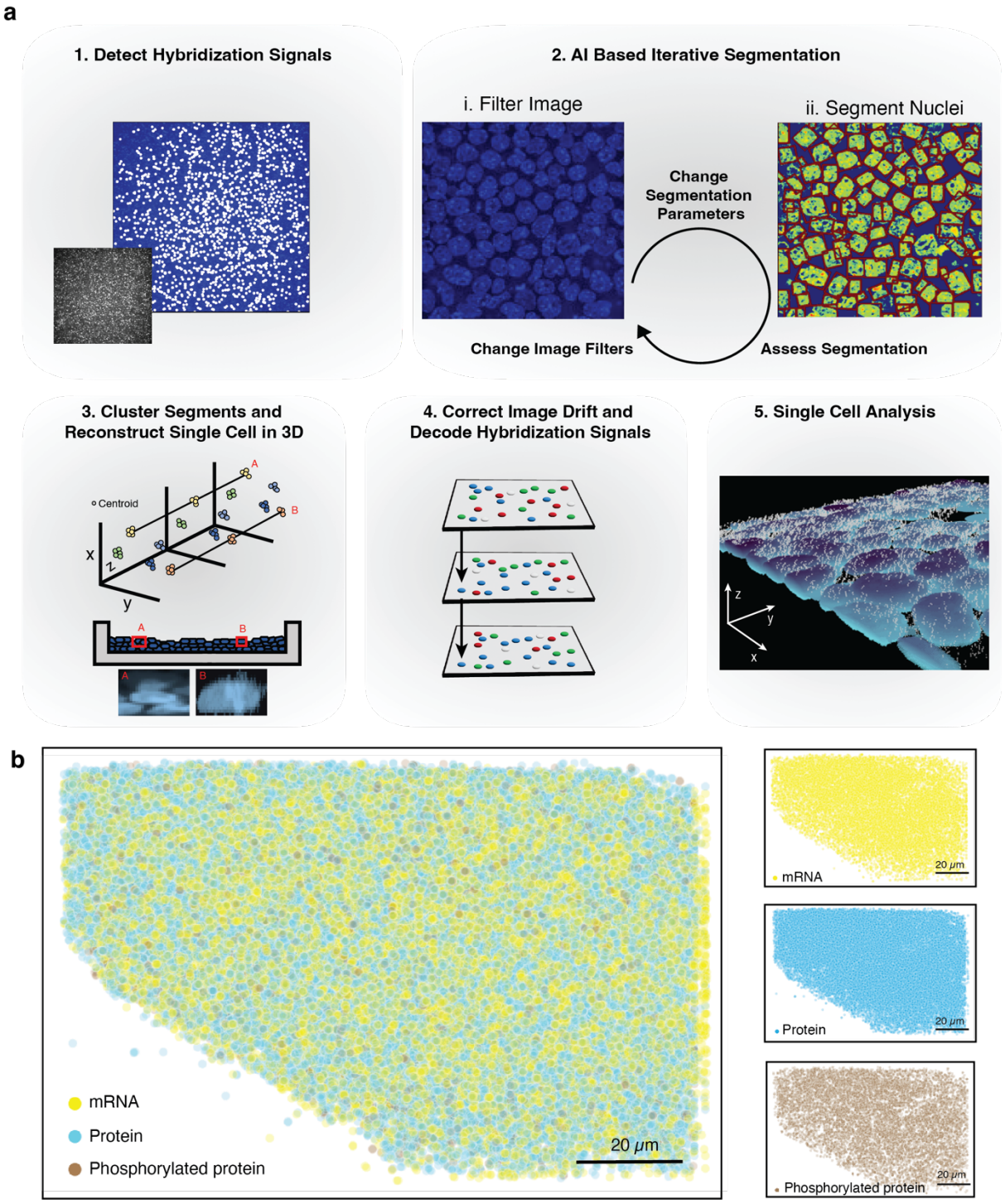


**Fig. 2: Computational outline of ARTseq-FISH. a,** A condensed summary of the automated computational pipeline that converts the raw microscope images into a single cell dataset, providing the abundance of each target per cell. First the hybridization signal is detected, followed by an iterative AI based segmentation approach, the segments are clustered, and the cells are reconstructed in 3D. Next, an image drift correction is applied to align the hybridization between rounds. In the final step these hybridization signals are decoded and assigned to the targets as well as individual cells. **b,** Reconstructed images show all the detected molecules in the cells cultured on micropattern 48 hours after leukemia inhibitory factor (LIF) withdrawal. The spots are subdivided into three classes: mRNA (yellow), protein (blue) and phosphorylated protein (brown). Scale bar, 20 µm.

**ARTseq-FISH profiles the expression of mRNAs, proteins, and phosphoproteins in individual mESCs**

We utilized ARTseq-FISH to explore how the expression of mRNAs and (phospho-)proteins is affected during the early stages of differentiation on micropatterns. LIF/serum cultured mESCs are heterogenous (Supplementary Fig. 22), due to their pluripotent nature, enabling them to make different cell fate decisions upon LIF withdrawal[52-54]. Therefore, we plated mESCs directly on a 750 µm diameter micropatterns and withdrew LIF from the serum medium for up to 48 hours to allow for cells to exit pluripotency. Notably, cells cultured under this condition are not the same as the cells primed to epiblast-like cells (EpiLCs)[12]. After fixation, we performed ARTseq-FISH on the micropatterned mESCs. Using our analysis pipeline, we visualized the locations of unique mRNA and (phospho-)protein targets (Fig. 3a) and quantified the abundance of 67 targets in individual cells (Fig. 3a-d). When discussing the protein targets detected using the respective antibodies (Supplementary Table 2), it is important to note that these measurements likely represent the total amount of protein detected, which includes both the unmodified and modified forms. Conversely, phosphorylated proteins were detected with specific antibodies (**protein* or phos-*protein* in figures).

Among protein targets, lineage-associated markers i.e., N-Cadherin, FOXA2, GATA6, showed higher abundance than pluripotency-related markers, i.e., NANOG, OCT4, and SOX2. Although we cannot rule out that these differences are due to dissimilarities in antibody efficiency, this is expected in mESCs that are exiting pluripotency (Fig. 3b)[10, 12, 15]. Notably, while RB shows low spot counts at a protein level, its mRNA and Phos-RB display higher spot counts (Fig. 3b-d), indicating that the difference in spot count between total RB and Phos-RB is caused by differences in antibody specificity. As mentioned previously, similar to other omics methods that rely on antibodies[33, 34], ARTseq-FISH is dependent on the binding efficiency of primary antibodies (for proteins) and PLPs (for mRNAs). Therefore, we cannot compare absolute counts between species. However, strong correlation of target counts between four different biological replicates (Fig. 3f) demonstrate the high reproducibility of ARTseq-FISH (Supplementary Fig. 21 and SN2 Fig. 20).

In addition, after filtering out the low abundant RNA targets in single-cell RNA sequencing (scRNAseq) data, ARTseq-FISH and scRNAseq mRNA quantification showed a high correlation ($r^2$=0.73) (Fig. 3g). Finally, to ensure true signals were detected with the image analysis software since no fixed intensity threshold is implemented, we tested the software on three samples: i) samples that did not include any readout probes, i.e., negative control (Fig. 3e, top panel); ii) samples that included readout probes, i.e., true signal; and iii) an *in silico* merged image which combined samples i and ii. For the merged image the number of false positives decreased six-fold for all channels (Fig. 3e, bottom panel). This demonstrates that in the presence of true signal the false positive rate for the noisiest channel is <1%. Together these data indicate that ARTseq-FISH is a reproducible technique that should be implemented when comparing relative spatial or temporal changes in expression levels of mRNA and proteins.

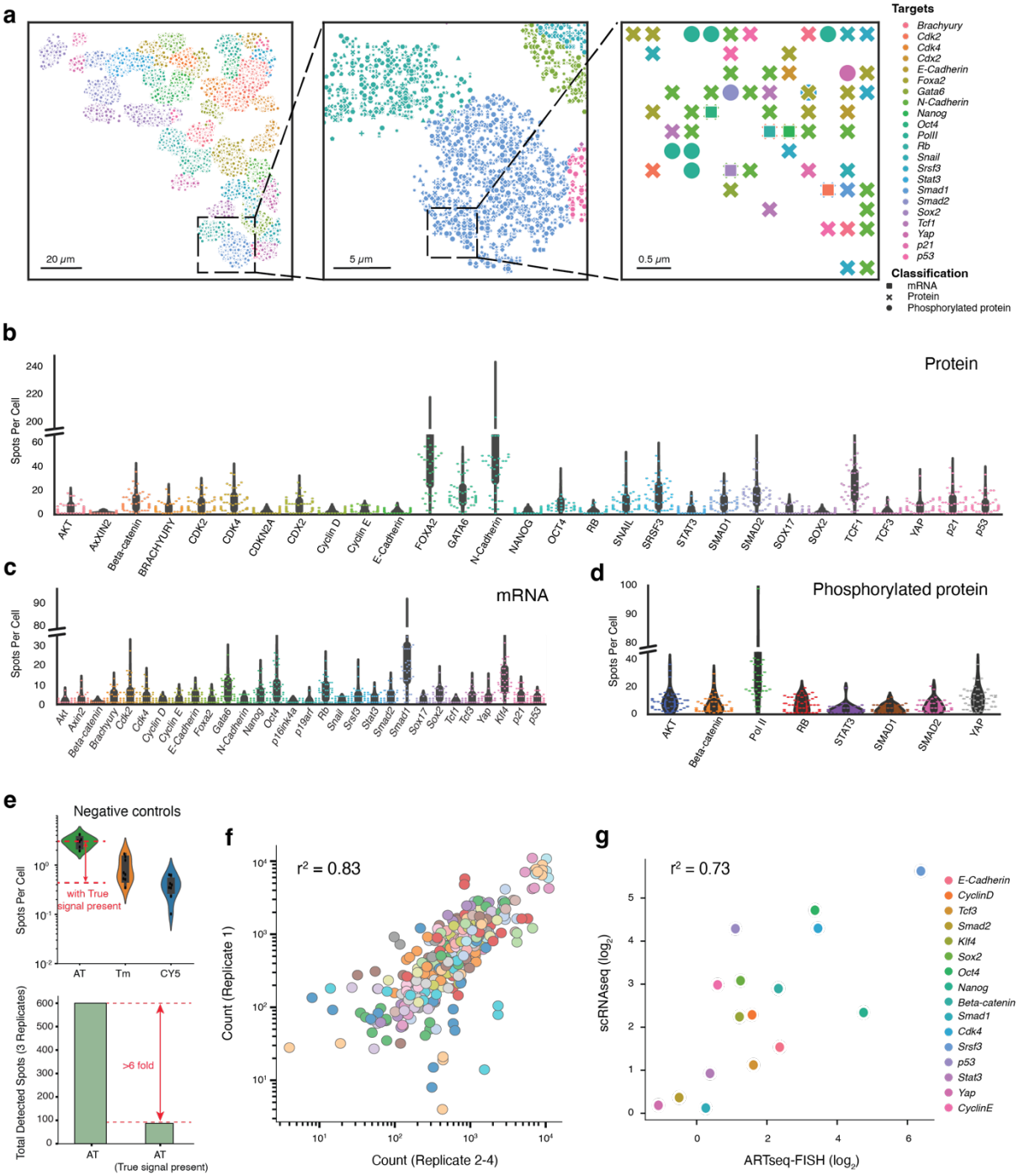


**Fig. 3: ARTseq-FISH profiles the distribution of mRNAs and proteins in individual mESCs on micropatterns. a,** Reconstructed images show the detected spots in Figure 2b assigned to individual cells and the identity of these targets at a specific location. Scale bar, 20 µm, 5 µm, and 0.5 µm. **b-d,** Quantification of the single cell count abundance of proteins (**b**), mRNAs (**c**), and phosphorylated proteins (**d**). 48 cells were analysed per target. **e,** Quantification of spots per cell for negative controls in three different channels (the three fluorophores are AT: Atto488, Tm: TAMRA, and CY5). Negative controls were performed without PLPs and 579 cells were analysed. When adding true signal to negative control images *in silico*, the detection of spots in the negative control decreases >6-fold for the green channel (bottom). **f,** The scatter plot shows the average correlation between the total count of individual targets detected within the image for 4 biological replicates at 48 hours differentiation of mESCs. **g,** The correlation of RNA targets per cell between ARTseq-FISH and scRNA-seq performed on serum/LIF cultured mESCs. scRNAseq data was analysed by Seurat[55]. 455, 503, 470, 482, 454, 466, 488, 408, 408, 408, 180, 241, 200, 200 and 233 non-micropatterned cells were analysed for *Smad2, Tcf3, E-cadherin, Cdk4, CyclinD, Smad1, Klf4, Oct4, Nanog, Sox2, p53, Beta-catenin, Stat3, CyclinE, Yap* respectively.

222

223 **ARTseq-FISH reveals gene expression gradients across micropatterned mESCs after 48**
224 **hours of LIF withdrawal**
225 ARTseq-FISH provides single cell quantification (Fig. 1-3) of each molecular species while
226 retaining spatial information. As confirmed by immunofluorescence, ARTseq-FISH data show
227 three patterns of molecular distribution across mESCs on micropatterns: i) increased expression
228 in cells located at the centre (i.e., p53); ii) evenly distributed throughout (i.e., phosphorylated
229 RNA Pol II); and iii) increased expressed in cells at the periphery (i.e., BRACHYURY) (Fig.
230 4a-f, Supplementary Fig. 23). Consistently, targets are classified into these three groups (Fig.
231 4e and Supplementary Fig. 24, purple, white, and orange respectively). Overall, lineage,
232 pluripotency as well as cell cycle associated proteins are more highly expressed in cells
233 localised towards the edge of the micropattern. Specifically, BRACHYURY and GATA6 are
234 mostly enriched in cells at the edge of the micropattern, as are the NANOG and SOX2 (Fig. 4e
235 and Supplementary Fig. 25a). Yet, BRACHYURY and GATA6 are not necessarily highly
236 expressed in the same cells as NANOG and SOX2 (Supplementary Fig. 25e). Surprisingly,
237 some mRNAs (i.e., *Stat3* and *Cdk2*) appear localised to the centre although their (phospho-
238 )protein counterparts are localised to the edge. This could either be because cells at the edge
239 are translationally more active and thereby require less mRNA to produce a higher amount of
240 protein. Alternatively, cells could be in the process of up or down regulating their mRNA, and
241 differences in mRNA and protein half-life could lead to a lack of correlation between the two
242 species[56]. Lastly, when calculating the mean fold change in expression level in cells located in
243 the centre versus edge, cells >125 μm from the edge were defined as being in the centre of the
244 micropattern (Supplementary Fig. 24), which is possibly an oversimplification. For example,
245 *Smad2* and *Rb* mRNA and protein are enriched in cells at the edge while our analysis suggests
246 that the phosphorylated proteins are more homogeneously expressed across the micropattern
247 (Fig. 4e). However, when quantifying the average expression profile of spots per cell at seven
248 positions across the micropattern, a reduction in Phos-RB and Phos-SMAD2 protein at the
249 centre (~375μm from the edge) of the micropattern becomes evident (Supplementary Fig. 25b-
250 d). Consequently, the localisation analysis likely masks more subtle changes in gene expression
251 between cells at the edge and centre of the micropattern.
252
253 To more closely examine the relationship between target expression levels and cellular
254 location, we quantified the expression levels of some targets in individual cells and plotted
255 these against cellular position on the micropattern. This analysis revealed that targets that are
256 more highly expressed in cells at the edge (i.e., BRACHYURY), display more of an
257 exponential trend (Fig. 4g), rather than linear. Conversely, some targets that are classified as
258 localised towards the centre (i.e., Phos-RB) or the edge (i.e., *Smad1* mRNA) appear to be most
259 highly expressed in cells located ~150 μm from the edge, rather than 375 μm from the edge,
260 the latter being the true centre. Interestingly, the single-cell expression levels of individual
261 targets are highly heterogeneous (Fig. 4g). While this could be a technical consequence of
262 ARTseq-FISH, the heterogeneity of p53, Phos-PolII, and BRACHYURY is also visible with
263 regular immunofluorescence (Fig. 4b), and mRNA levels have previously been reported to
264 become more heterogeneous as cells exit pluripotency[57]. Furthermore, we have shown that the
265 mean gene expression values are reproducible across replicates when quantified by ARTseq-
266 FISH (Fig 3f). Therefore, this heterogeneity is likely biological and indicates that although
267 cellular location on the micropattern does generate trends in gene expression profiles, both
268 mRNA and protein synthesis is still heterogenous after 48 hours of LIF withdrawal.

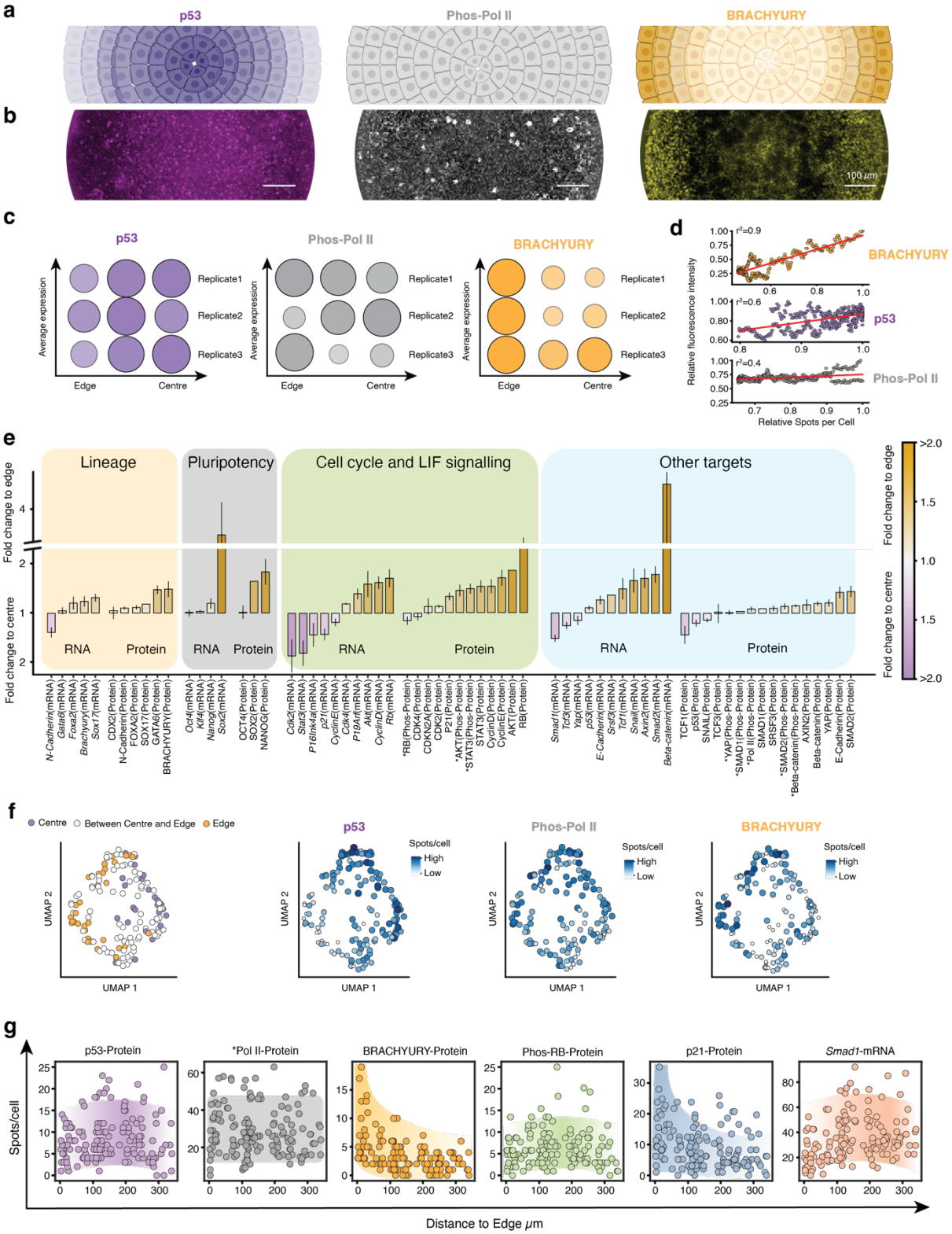


**Fig. 4: ARTseq-FISH reveals gradients of mRNA and protein expression levels within micropattern-differentiated mESCs.**

**a,** Schematic illustration of three representative spatial distributions of molecules on micropatterns. Created with BioRender.com. **b,** Immunofluorescence results of p53, Phos-Pol II (Phosphorylated RNA Pol II), and BRACHYURY within a micropattern-differentiated mESCs. Scale bar, 100 µm. **c,** Average expression profile of spots per cell at different positions on the micropattern (edge to centre) for p53, Phos-Pol II, and BRACHYURY proteins from 3 biological replicates (150, 125, and 158 cells and 1 micropattern were per replicate). **d,** Pearson correlation between relative mean fluorescence in **(b)** and relative spots per cell with respect to their position on the micropattern **(c)**. **e,** Mean fold change of the expression level of individual targets between the edge and centre

(purple and orange respectively) of the micropattern across 3 biological replicates (125-158 cells and 1 micropattern analysed per replicate). *: phosphorylated protein. Error bars represents SEM of 4 biological replicates. **f,** UMAP of cells after 48 hours of LIF withdrawal, with the colour representing if cells are localised towards the edge (orange) or centre (purple) of the micropattern (left). Same UMAP with single cell expression level of p53, Phos-Pol II, and BRACHYURY proteins indicated in blue. 158 cells and 1 micropattern were analysed. **g,** The spots per cell (y-axis) with respect to the position of the cell on the micropattern (x-axis) of selected targets. The edge of the micropattern serves as the reference value for the relative position of the cells. Cells are found at the edge at 0 µm and near the centre at 375 µm. 158 cells were analysed per target.

**Position-dependent mRNA and protein profiles emerge over time**

To investigate how mRNA and protein abundance changes over time, we examined the spatial distribution of molecules in micropatterned cells at different time points (0 hours, 12 hours, 24 hours, and 48 hours) following LIF withdrawal (Fig. 5a). To better understand the changes, we grouped targets into different categories (Supplementary Table 5) and quantified the relative changes in target abundance across the micropattern in 2D (Fig. 5b) over the 48-hour LIF withdrawal period. At the initial time point (0 hours), both RNA and protein levels across the different categories showed a relatively homogeneous distribution. Interestingly, we noticed a specific region, approximately 150 µm from the edge of the micropattern, where mRNAs related to cell cycle class 2 (genes that promote cell cycle progression) were elevated (Fig. 5c, cell cycle class 2). Moreover, this region exhibited slightly increased levels of mRNAs and proteins related to (LIF) signalling at 0 hours (Fig. 5c, signalling). While we considered that this might be an artefact of initial uneven cell seeding, cells were seeded on the micropattern 24 hours before LIF withdrawal (i.e., at T = -24 hours). Therefore, these subtle initial expression differences could be indicative of first changes in position-based expression profiles. This is reinforced by two distinct areas on the micropattern emerging where both mRNA and protein levels tended to increase over time: these were found at position 2 and 6 of the micropattern, located approximately 150 µm from either side of the edge (Fig. 5b).

To further explore whether proteins are expressed differently based on cellular location on the micropattern, we quantified gene expression profiles for individual cells situated either at the true edge or at the true centre of the micropattern (Fig. 5b). Once again, we categorized targets based on their functions and plotted the relative single-cell changes over the 0, 12, 24, and 48 hours of LIF withdrawal. At 0 hours, cells at the micropattern's edge contain higher levels of proteins associated with cell cycle 1 (lengthening G1) than at the centre (Fig. 5d, 0h cell cycle 1 top compared to bottom). Subsequently, at the edge after 12 hours we observed a decrease in proteins associated with cell cycle 1 (lengthening G1) and an increase in proteins related to cell cycle 2 (cell cycle progression) (Fig. 5d). These findings suggested that within the first ~12 hours of LIF withdrawal, cells at the edge alter the expression of genes associated with cell cycle progression, potentially leading to higher proliferation rates during this time. In contrast, at the micropattern's centre, the levels of cell cycle 1 (lengthening G1) increases already from 0-12 hours, while cell cycle 2 genes (cell cycle progression) initially remain constant (Fig. 5d, bottom). These results indicated that, the G1 phase of cells located at the centre might start increasing 0-12 hours after LIF withdrawal.

When analysing genes associated with pluripotency and particular lineages, we only observed slightly different gene expression profiles at the centre compared to the edge of the micropattern. Proteins that exhibit the most significant differences in expression profiles are SOX17, BRACHYURY, (Fig. 5d, right) and NANOG (Fig 5e, left). In particular, SOX17 levels increase mostly between 0-12 hours at the edge of the micropattern, while at the centre there is a more gradual increase over the course of 48 hours of LIF withdrawal. BRACHYURY levels increase gradually at the edge of the micropattern from 12-48 hours of LIF withdrawal

330 and remain relatively constant at the centre. Lastly, NANOG levels increase from 0-12 hours
331 and decrease again from 12-24 hours of LIF withdrawal at the edge of the micropattern. In
332 contrast, at the centre of the micropattern NANOG levels increase from 12-24 hours of LIF
333 withdrawal.
334
335 To validate these findings, we performed time-lapse microscopy on micropatterned NANOG-
336 GFP mESCs[58, 59] for 46.5 hours of LIF withdrawal (Fig 5e, right). When quantifying the mean
337 NANOG-GFP intensity for different positions at the edge and the centre of the micropattern,
338 we observed distinct NANOG-GFP expression changes. Specifically, cells at the edge of the
339 micropattern show an initial increase in NANOG-GFP expression (lasting ~12-15 hours)
340 followed by a gradual decrease in NANOG-GFP expression. Conversely, the centre of the
341 micropattern displays a decrease in NANOG-GFP expression from 15-20 hours post LIF
342 withdrawal, followed by a continuous increase in NANOG-GFP expression (Fig 5e, right).
343 While the overall trend at the edge is consistent with ARTseq-FISH NANOG data (Fig 5e, left,
344 orange), the initial decrease observed in the time-lapse experiment for cells at the centre of the
345 micropattern is not visible by ARTseq-FISH (Fig. 5e, left, purple). This could be because
346 ARTseq-FISH reveals expression levels of cells that are fixed after 0, 12, 24, and 48 hours post
347 LIF withdrawal and do not represent a true time-course, which might conceal rapid changes in
348 expression levels. Furthermore, the time-lapse experiment was not analysed at a single-cell
349 level. Alternatively, it is possible that the differences between the time-lapse experiment and
350 ARTseq-FISH are cell-type specific. Therefore, we sought to confirm the expression of another
351 pluripotency marker (OCT4) by immunofluorescence at 0 and 48 hours of LIF withdrawal,
352 which shows similar behaviour as ARTseq-FISH (Supplementary Fig. 26).
353
354 Interestingly, at the single-cell level, we found a negative correlation between pluripotency-
355 associated proteins (i.e., OCT4 and SOX2) and lineage-associated markers (i.e., FOXA2,
356 GATA6 and SOX17) (Fig. 5f) in cells at the edge of the micropattern. This indicates that cells
357 at the edge are not uniform in their protein expression levels. When we project the data on a
358 2D UMAP, we observe the most prominent separation of cellular expression profiles occurring
359 between 0-12 hours post LIF withdrawal (Fig. 5g). Furthermore, while there is some separation
360 in cells located at the edge and centre, this separation is subtle, and predominantly visible at 48
361 hours post LIF withdrawal (Fig. 5g).
362

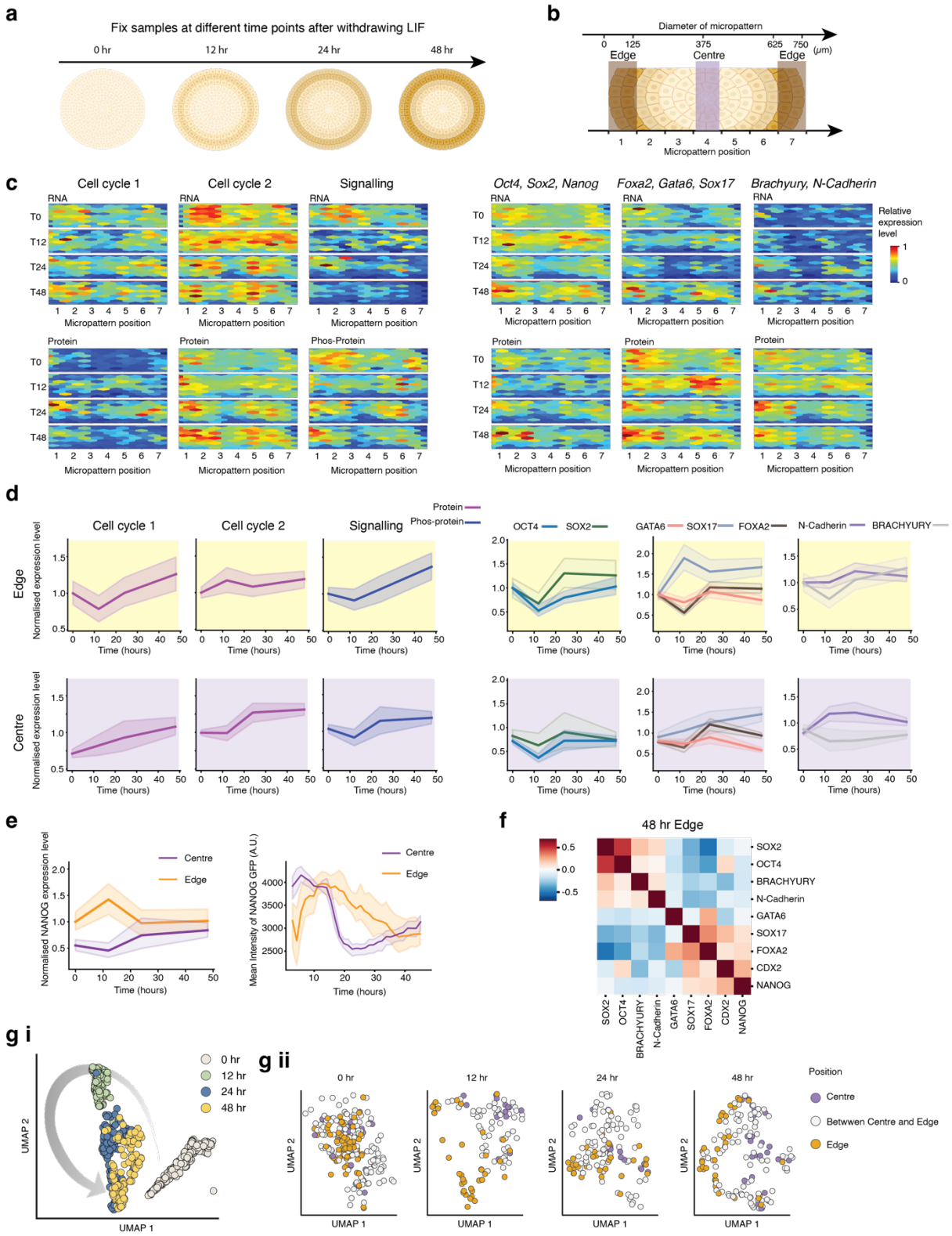


**Fig. 5: Spatial-temporal quantification of mRNAs and proteins after LIF withdrawal from mESCs on micropatterns. a,** Schematic of the experiment where ARTseq-FISH was performed at 0, 12, 24 and 48 hours after LIF withdrawal. Created with BioRender.com. **b,** Schematic of the definition of centre and edge on the micropattern. Created with BioRender.com. **c,** Heatmap showing the abundance of different classes of targets (see Table S5 for full list of targets) across 1 micropattern at 0, 12, 24 and 48 hours after LIF withdrawal. The expression level of targets is normalised to the maximum abundance across all four time points. **d,** Relative single cell expression levels of the targets shown in **c**, at the edge (top) and the centre (bottom) of the micropattern at 0, 12, 24 and 48 hours after LIF withdrawal. 0–24-hour data includes 2 biological replicates; 48 hours includes 3 biological replicates (for the edge 393 cells and the centre 238 cells were analysed in total). For each replicate and

373 time point 1 micropattern was analysed. Shaded regions represent 95% confidence intervals. **e,** Single cell
374 NANOG protein expression at the edge and centre of micropattern at 0, 12, 24 and 48 hours after LIF withdrawal
375 detected by ARTseq-FISH (left). 0–24-hour data includes 2 biological replicates; 48 hours includes 3 biological
376 replicates (edge and centre include 393 and 238 cells in total respectively). For each replicate and time point 1
377 micropattern was analysed. Quantification of live cell time-lapse of NANOG-GFP positive mESCs for 5 different
378 positions at the edge (cells) and the centre (cells) of 1 micropattern over 46.5 hours of LIF withdrawal (right).
379 Shaded regions represent 95% confidence intervals. **f,** Pearson correlation and hierarchical clustering of
380 pluripotency and lineage related markers at the edge of the micropattern (3 biological replicates, 1 micropattern
381 each, 111 cells total) at 48 hours after LIF withdrawal. **g (i)** UMAP clustering of the individual cells within a
382 single micropattern experiment at different time points (0, 12, 24 and 48 hours) after LIF withdrawal. **(ii)** UMAP
383 clustering of single cells at different positions (centre, edge or between centre and edge) within the micropattern
384 (purple, orange, and white respectively). 1 biological replicate and 1 micropattern (0, 12, 24 and 48 hours include
385 269, 139, 141, 158 cells respectively).
386
387
388 **Cellular location on the micropattern impacts proliferation**
389 In light of the gene expression profiles (Fig. 5c) indicating differences in protein signals
390 between the micropattern's edge and centre, we proceeded to investigate the translational
391 activity of cells across the micropattern. To do this, we exposed micropatterned mESCs to the
392 puromycin analogue O-propargyl-puromycin (OPP), which is incorporated into newly
393 synthesized proteins[60]. Through click chemistry, we fluorescently labelled the nascently
394 translated polypeptides (Fig. 6a). Our data revealed a gradual decrease in protein synthesis
395 across the entire micropattern over time (Fig. 6b). Notably, the signal in the micropattern's
396 centre decreased more readily, particularly after 24-48 hours (Fig. 6b-c, light and dark green).
397 These findings are in line with ART-seqFISH data, showing more prominent protein detection
398 at the micropattern's edge after 48 hours of LIF withdrawal (Fig. 6d). These data suggest that
399 spatial organization plays a role in the dynamics of translational activity in micropatterned
400 mESCs.
401
402 To gain insights into why translation might be reduced in the centre of the micropattern, we
403 next tried to determine if cells proliferate differently depending on their position on the
404 micropattern. To this end, we first quantified cell density across the micropattern as a function
405 of DAPI intensity. Interestingly, on our 750 µm diameter micropatterns, cell density shows two
406 radially symmetric peaks over time, approximately 100 µm from the edge of the micropattern
407 (Fig. 6e-f), indicating that the colonies are not flat but somewhat 'donut' shaped (Fig. 6g). To
408 determine if these differences in cell density were caused by increased proliferation, we
409 performed EdU staining after 0, 12, 24 and 48 hours of LIF withdrawal and quantified cell
410 proliferation from the incorporation of EdU into newly synthesized DNA[61] (Fig. 6h). The
411 results indicate that there are fewer cells in the S phase at the centre of the micropattern than
412 towards the edge and therefore likely display reduced proliferations already after 12 hours of
413 LIF withdrawal (Fig. 6i). Interestingly, at the very edge of the micropattern there still appear
414 to be cells incorporating EdU after 48 hours of LIF withdrawal. To confirm that actively cycling
415 cells are more abundant at the edge of the micropattern after LIF withdrawal, we performed
416 Ki-67 staining[62] (Fig. 6j and Supplementary Fig. 27), an indirect marker for proliferating cells.
417 The data show that at 0 hours after LIF withdrawal Ki-67 staining is mostly homogenous across
418 the micropattern, indicating comparable cell cycling at the centre and edge of the micropattern
419 (Fig. 6i). Notably, at 0 hours there is reduced Ki-67 signal at the very centre of the micropattern
420 (micropattern position 1 and 8), consistent with quantified EdU signal (Fig. 6i, light blue).
421 From 0 to 12 hours, there appears a slight increase in Ki-67 intensity (i.e., cell cycling) at the
422 centre of the micropattern, which subsequently drops from 24 to 48 hours post LIF withdrawal,
423 demonstrating a decrease in cellular proliferation or a state of cell cycle arrest (Fig. 6j and
424 Supplementary Fig. 27). Caspase-3 and 7-AAD staining as well as nuclear morphology

analysis indicate that this lack of proliferation could be connected to increased apoptosis at centre of the micropattern[63] (Supplementary Fig. 28). Conversely, at the edge of the micropattern cells show more consistent Ki-67 intensities over time (Fig. 6j), although at 48 hours the cells at the very edge (micropattern position 1 and 8), do not show increased cycling as would be expected from the EdU staining (Fig. 6j compared to Fig. 6i), this could be because Ki-67 is less sensitive, in particular for cells with a short G1 phase[64]. Nevertheless, these combined assays indicate that cells positioned more towards the edge of the micropattern proliferate more readily than cells at the centre.

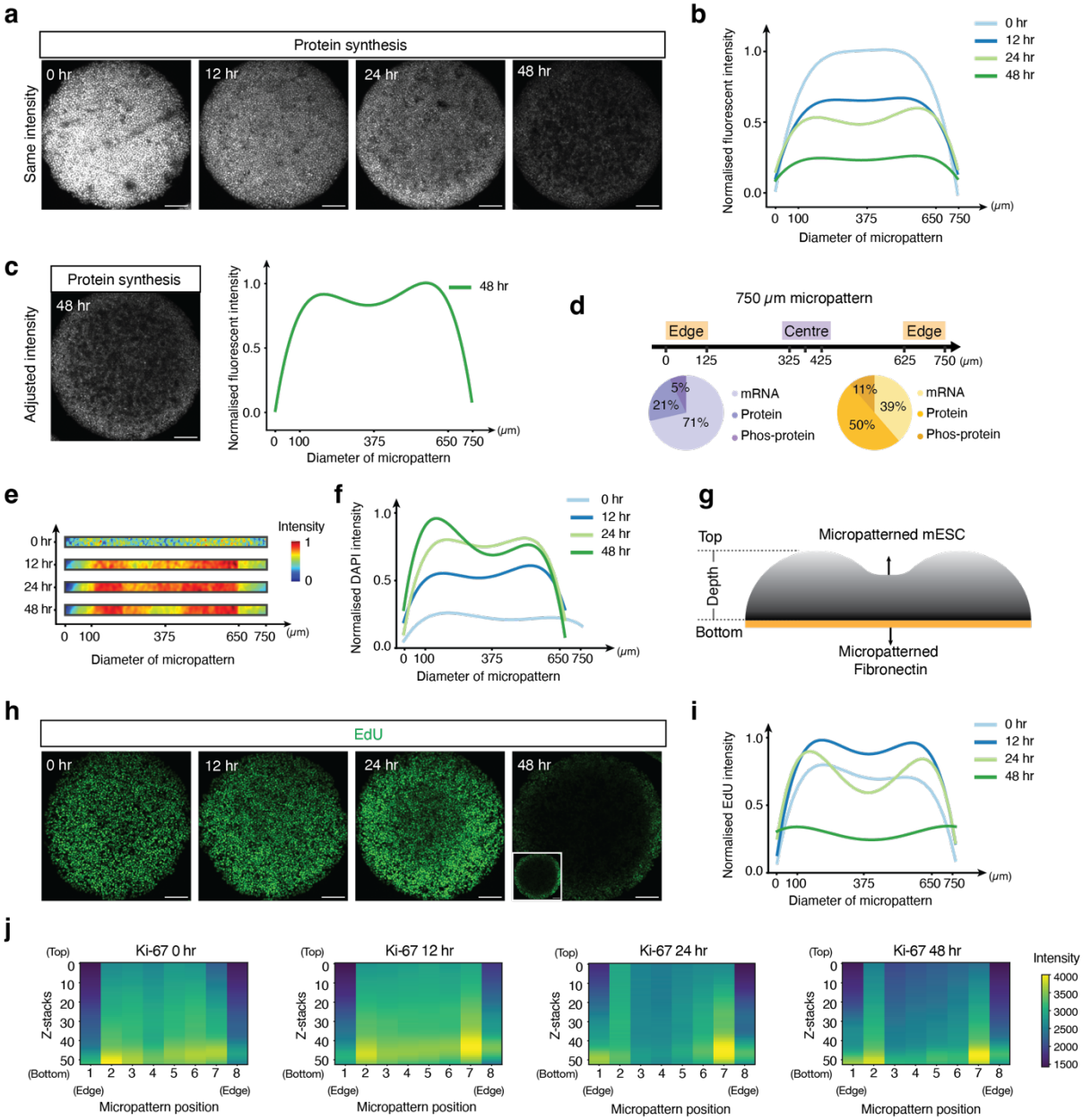


**Fig. 6: mESCs display position-dependent differences in protein synthesis and proliferation rates.** **a,** Representative images showing the protein synthesis of the micropatterned mESCs at 0, 12, 24 and 48 hours after LIF withdrawal. Images from different time points are set as the same maximum and minimum gray value. Scale bar, 120 µm. **b,** Quantification of relative fluorescent intensity of the protein synthesis in mESCs across 2-10 micropatterns at 0, 12, 24 and 48 hours after LIF withdrawal. **c,** Representative images showing the protein synthesis of the micropatterned mESCs at 48 hours after LIF withdrawal (left). Scale bar, 120 µm. Quantification of relative fluorescent intensity of the protein synthesis in mESCs across 10 micropatterns at 48 hours after LIF withdrawal (right). **d,** Pie chart showing the percentage of mRNAs, proteins, and phosphoproteins of targets that are more abundant at the centre (purple) and targets that are more abundant at the edge (orange) of the

micropattern. **e and f,** Heatmap of DAPI intensity across the micropattern and normalized DAPI intensity across the micropattern at 0, 12, 24 and 48 hours after LIF withdrawal. **g,** Schematic shows the "donut" shape of the micropatterned mESCs. **h,** Representative images showing EdU staining of the micropatterned mESCs at 0, 12, 24 and 48 hours after LIF withdrawal. Images from different time points are set as the same maximum and minimum grey value. Insets: image of EdU staining at 48 hours after LIF withdrawal with adjusted contrast. Scale bar, 120 μm. **i,** Quantification of relative fluorescent intensity of EdU staining in mESCs across 2-10 micropatterns at 0, 12, 24 and 48 hours after LIF withdrawal. **j,** Heatmap of Ki-67 expression level at z-projection across 1 micropattern at 0, 12, 24 and 48 hours after LIF withdrawal.

## Cellular location on the micropattern impacts cell cycling dynamics

Given the distinct expression profiles of cell cycle-related genes observed between cells at the micropattern's edge and centre using ARTseq-FISH (Fig. 5d), we aimed to quantitatively analyse cell cycle progression on a single-cell basis. To this end, we conducted time-lapse microscopy on micropatterned Fucci mESCs[65, 66], which enable the visualisation of cell cycle dynamics in live cells (Fig. 7a). Single-cell tracking and measurement of Azami Green (Az1) and Kusabira Orange-2 (KO-2) fluorescence over time delineates the individual stages of the cell cycle (Fig. 7b-c). We performed single-cell tracking of 35 cells across the micropattern (20 at the centre and 15 at the edge) over a 45-hour period following of LIF withdrawal. When assessing the length of the G1 phase at different time intervals post LIF withdrawal, intriguing differences emerge between cells at the micropattern's edge and those at the centre. Specifically, cells at the micropattern's centre that enter the G1 phase within the initial 5 hours of LIF withdrawal consistently exhibit a relatively short G1 phase of approximately 3 hours (Fig. 7d, top and Supplementary Fig. 31a, left). Conversely, cells that enter the G1 phase after this initial 5-hour period show a notably extended G1 phase (Fig. 7e). Markedly, cells at the micropattern's edge display a G1 phase duration similar to cells at the centre (Fig. 7d, bottom and Supplementary Fig. 31a, middle). However, a subset (about 25%) of cells at the edge already exhibit a prolonged G1 phase within the first 5 hours of LIF withdrawal (Supplementary Fig. 31a, right). Similarly, after the initial 5-hour period, just over half (approximately 60%) of cells closer to the edge continue to cycle, while the remaining portion (about 40%) display an extended G1 phase (Fig. 7f). These single-cell analyses show that the G1 phase of cells at the centre gradually elongates, while >half of the cells at the edge continue cycling until ~30 hours post LIF withdrawal. These data suggested that the cell cycle pace is more heterogeneous at the edge of the micropattern than at the centre.

We next performed a more comprehensive population-based analysis spanning the entire micropattern over the course of the 45-hour LIF withdrawal. By comparing the proportion of cells in G1 versus S/G2/M phases for cells at the micropattern's edge and centre over time, we again observe a subtle yet discernible difference (Fig. 7g). Specifically, in the centre there was a gradual decline in the fraction of cells in S/G2/M phase, beginning approximately 6 hours post LIF withdrawal (Fig. 7g, left). Instead, cells at the edge of the micropattern show a relatively unchanged distributions across the cell cycle stages over time, with the proportion of cells in the S/G2/M phase only declining after ~40 hours of LIF withdrawal (Fig. 7g. right). Since these data align with the single-cell analysis, the latter is likely representative of the full population. Furthermore, these findings are consistent with the Ki-67 staining results (Fig. 6j and Supplementary Fig. 27) and the cell cycle stages quantified from DAPI intensity differences[67-69] (Supplementary Fig. 29-30). Although differences in timing of these changes might arise because the Fucci mESCs are a separate cell line[65, 66], the fraction of cells in the late S/G2/M phase (Fucci mESCs) follow a similar trend to the EdU staining performed on mESCs (Fig. 7h). Lastly, single cell tracking of both NANOG-GFP and Fucci mESCs suggests that cell migration is minimal (Supplementary Fig. 31b and c, respectively). While the potential for rapid cell migration that elude cell tracking exists, the prevailing data indicates that cells

remain either at the centre or the edge of the micropattern (Supplementary Fig. 31c). Collectively, the data indicate that cells closer to the micropattern's edge exhibit increased proliferation compared to those at the centre, evident 5-24 hours after LIF withdrawal.

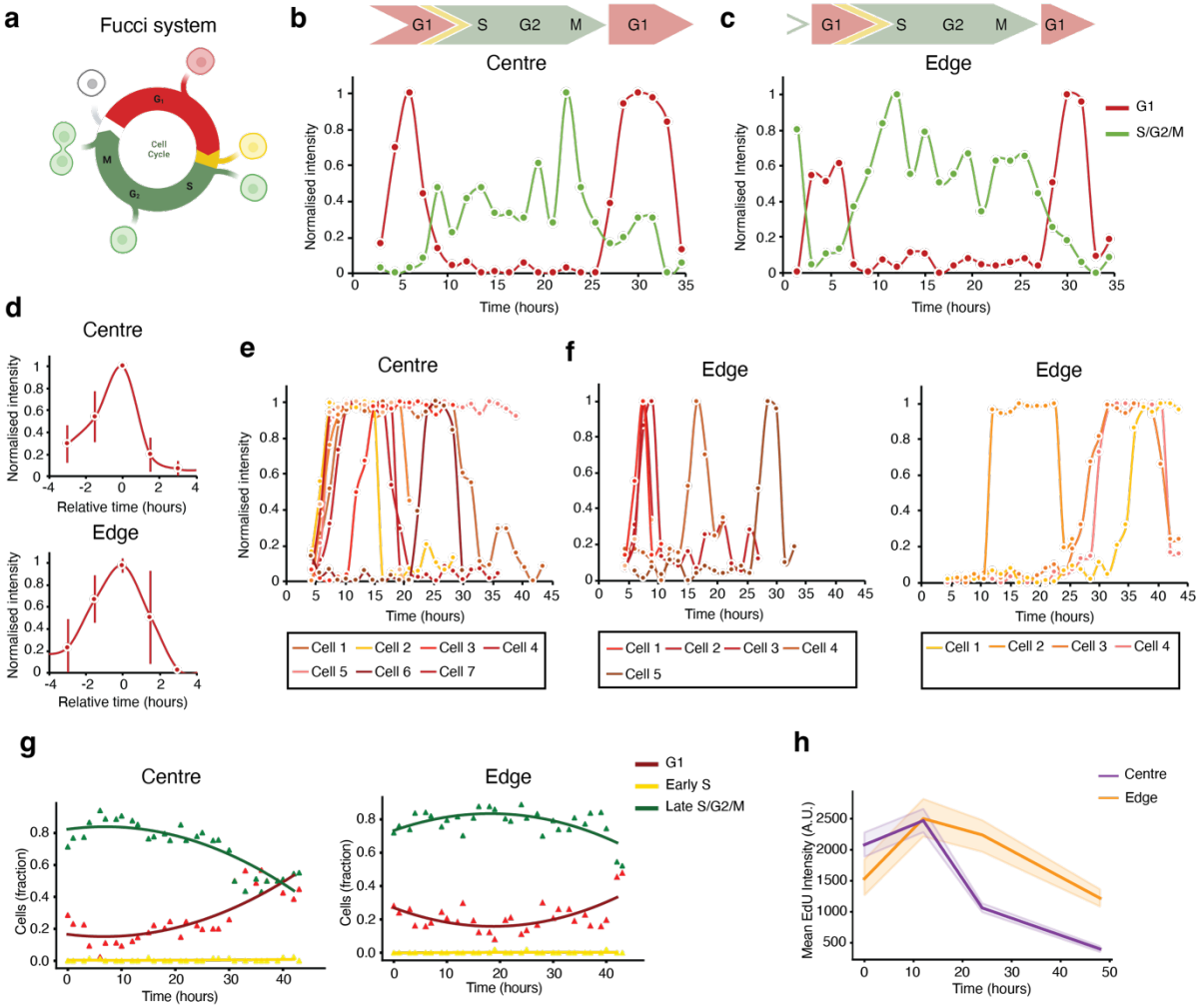


**Fig. 7: Live cell imaging reveals differences in cell-cycle progression.**
**a,** Schematic illustration of the Fucci mESCs demonstrating different colours at different cell cycle stages. Created with BioRender.com. **b-c,** Kusabira Orange-2 (KO-2) (G1) and Azami Green (Az1) (S/G2/M) intensity of a tracked cell in the centre (**b**) and edge (**c**) of the micropattern. **d,** Average KO-2 intensity throughout the G1 phase for cells at the centre (top) and edge (bottom) of the micropattern that enter G1 within 5 hours of LIF withdrawal. Average is of 12 cells for the centre and 6 cells for the edge. Error bars represent standard deviation. **e-f,** Single cell KO-2 (G1) traces of cells that enter G1 after 5 hours of LIF withdrawal at the centre (**e**) and edge (**f**) of the micropattern. 7 (centre) and 9 (edge) cells were analysed respectively. **g,** Quantification of the fraction of G1, early S, and late S/G2/M mESCs at the centre (left) and the edge (right) of the micropattern over time after 45 hours of LIF withdrawal. 1961 cells at the edge and 2190 cells at the centre were analysed in total. **h,** Quantification of mean EdU intensity of mESCs for 10 different positions at the edge and the centre of 1 micropattern at 0 hours, 12 hours, 24 hours, and 48 hours after LIF withdrawal. Shaded regions represent 95% confidence intervals.

## Discussion

Thus far, there have been two major areas of focus when studying micropatterned cells: i) implementation of immunohistochemistry (IHC) to determine spatial-temporal protein abundance in low throughput[10-15]; or ii) revealing the emergence of specific cell types by single-cell transcriptomic sequencing in high throughput[15]. Here we developed and exploit a

technique that provides quantitative spatial information on different functional proteins and their respective mRNAs at same time.
ARTseq-FISH, enables simultaneous measurement and quantification of relative mRNA and (phospho-)protein abundance in individual cells. The combined protocol of mRNA and protein detection provides the same resolution of different molecular species and is scalable (Fig. 1). Additionally, the deep learning-based image analysis pipeline in ARTseq-FISH (Fig. 2) identifies the cellular nucleus and FISH signals, which allowed detection of 67 mRNAs, proteins, and phosphoproteins simultaneously (Fig. 3). We applied ARTseq-FISH to identify position-dependent gene expression profiles on micropatterned mESCs (Fig. 4). The analysis revealed the expression levels of individual cells and their dependence on the respective location on the micropattern during 48 hours of LIF withdrawal. Intriguingly, cells located at the edge and centre of the micropattern obtain different gene expression profiles over time (Fig. 5) while maintaining a high degree of cell-to-cell variability in expression levels. We demonstrate that depending on the micropattern location, cells display differences in protein synthesis, cell cycling and proliferation (Fig. 6-7). Taken together, our findings indicted that while gene expression is still highly heterogeneous differences in mRNA and protein levels emerge as early as 12 hours after LIF withdrawal.

While other impressive spatial-omics methods that simultaneously measure mRNA and proteins exist (DSP[18] and SMI[36], introduced by NanoString; π-FISH[70]), we focused on developing a protocol that allows for a combined amplification step yielding comparable resolution for mRNA and protein detection. This combined detection and analysis for mRNA and protein offers the opportunity to circumvent the challenges in integration of different datasets[71-73]. Since the sensitivity of ARTseq-FISH relies on the antibodies (for proteins) and PLPs (for mRNAs), similar limitations apply compared to existing methods[33, 34, 41, 43]. Although there is a risk that the affinity of the antibodies may be influenced by the conjugation method, it is a widely used procedure in current proteomic technologies[33-35]. While we have shown that the detection efficiency of the PLP-based method depends on the binding efficiency of the chosen padlock probe sequence, we only used one PLP to target each mRNA in this study. This is feasible, when comparing relative RNA abundance, either between individual cells (similar to scRNA-seq) or as we do here between different locations or different time points during the initial stages of mESCs differentiation.

In future, ARTseq-FISH has the potentials to detect thousands of targets simultaneously by introducing more unique readout probe sequences and maximizing the hybridization rounds. For instance, to detect 2048 targets, we will need 40 different readout probe sequences and at least 10 rounds of hybridization. However, in theory sequential FISH methods are able to perform 81 hybridization rounds, which would allow the detection of more than 10,000 targets with ARTseq-FISH. Yet, to achieve this, it will be critical to assign different hybridization rounds to high abundance targets to avoid optical crowding. A future application of ARTseq-FISH lies specifically in capturing the spatial information of different molecular species (i.e., mRNAs, proteins, phosphoproteins) and quantifying their relative abundance in particular biological processes. One of the advantages of using padlock probes is the power of signal amplification by RCA. Therefore, ARTseq-FISH has the potential to detect DNA (i.e., single nucleotide polymorphisms (SNPs))[74], miRNAs[75, 76], viral RNA[77], and proximity of proteins[37, 78] or even proximity of RNA and protein. In addition, due to the signal amplification of RCA, the results of ARTseq-FISH can also be read out by flow cytometry[79, 80], which makes this and future techniques more broadly accessible.

## Methods

### Cell culture

mESC-E14 (mESCs) in this study were obtained from Hendrik Marks's group at Radboud University[81]. The culture plates were coated with 0.1% gelatin (Sigma Aldrich, 48723-500G). Undifferentiated mESCs were cultured and maintained in the medium consisting of high glucose-Dulbecco's Modified Eagles Medium (Gibco™, 41965039) supplemented with 15% fetal bovine serum (Gibco™, A3840002), 2 mM L-glutamine (Gibco™, A2916801), 1 mM sodium pyruvate (Gibco™, 11360039), 1% penicillin–streptomycin (Gibco™, 15140122), 0.1 mM beta-mercaptoethanol (Gibco™ 31350010) and 500 U/mL recombinant leukemia inhibitory factor (LIF; Millipore, ESG1107) at 37 °C in 5% $CO_2$. Cells were passaged every 2-3 days using 0.05% Trypsin/EDTA (Gibco™, 25300062). Cell density was 5x $10^4$ per well for the experiments in the μ-Slide (ibidi, 81501) and 1x $10^4/cm^2$ for the experiments in the μ-Slide 3D perfusion (ibidi, 80376). For differentiation assays, cells were cultured on micropatterns in LIF medium for 1 day and then changed to a medium without LIF (-LIF) for up to 2 days.

### Micropatterned Substrate Fabrication

Micropatterned islands with different diameters (750 μm) were produced on a silicon mask using standard photolithography [82]. Distances between the microfeatures were 100 μm and the height of the microfeatures was between 50 μm and 100 μm. The PDMS and the curing agent (SYLGARD 184, 1.1KG) was mixed with a ratio of 10:1 in a plastic beaker. The PDMS mixture was degassed to remove the air bubbles under vacuum. Then, the degassed PDMS mixture was poured onto the master in a petri dish. A gel was formed in a 60°C oven over night. Finally, the gel PDMS stamps was peeled off the master.

The μ-Slide 3D perfusion microchambers were plasma oxidized to improve protein printing efficiency and cell attachment on the glass bottoms [83]. The surface of the PDMS stamps was placed with a drop of 50 μg/mL fibronectin in PBS and incubated for 1 hour at room temperature. The PDMS stamps were washed twice with PBS and dried thoroughly. The glass bottoms of μ-Slide 3D perfusion were then coated with the fibronectin from the PDMS stamps, followed by the graft of the PLL (20)-g [3.5]- PEG (2) (0.1 mg/mL, SuSoS AG) in 10 mM HEPES (Gibco™, 15630080) for 30 minutes at room temperature. The PLL-g-PEG prevents cell attachment in the nonprinted areas [84].

### Immunostaining

Cells were fixed with 4% paraformaldehyde (PFA) (Sigma Aldrich, 1040021000-1L) for 10 minutes at room temperature and then permeabilized with 0.5% Triton in 1x PBS at room temperature for 10 minutes. Cells were washed with 1x PBS three times after fixation and permeabilization. After permeabilization, cells were incubated in blocking buffer (5% BSA in 1x PBS containing 0.5% Triton) for 1 hour at room temperature. The primary antibodies were diluted in blocking buffer and incubated at room temperature for 2-4 hours. Cells were then washed with 1x PBS three times and incubated in secondary antibody solution for 2 hours at room temperature. The secondary antibodies were diluted 1:1000 in 1x PBS. DAPI (10 μg/mL) (Thermo Scientific™ 62247) staining was performed together with secondary antibodies.

For Ki-67 (Cell Signaling, 9192), Caspase-3 (Cell Signaling, 94530), OCT4 staining, the primary antibodies were diluted as recommended ratio in blocking buffer. The cells were then incubated overnight at 4°C in the primary antibody solution. The other steps of the protocol remained the same as above.

### smFISH

617 Probes of *Nanog* were purchased from Stellaris (LGC Biosearch Technologies, Novato, CA)
618 (http://www.singlemoleculefish.com/). Each set contains 28 probes and each probe is 20 nt
619 long (Table S1). Probes are conjugated with TAMRA. Cells were fixed with 4% PFA (Sigma
620 Aldrich, 1040021000-1L) for 10 minutes at room temperature and then permeabilized with pre-
621 chilled 70% EtOH at 4°C for a minimum of 1 hour. Cells were washed three times with 1x
622 PBS. Probes were diluted to a final concentration of 50 nM in 1 g/mL dextran sulfate (Sigma,
623 catalog # 42867), 2x SSC and 10% formamide (Invitrogen, AM9342). The hybridization of the
624 probes was performed overnight at 37°C. The next day, samples were washed with 2x SSC
625 buffer at 37°C for 30 minutes and then incubated with DAPI solution (diluted in 2x SSC) at
626 37°C for 15-20 minutes. Cells were washed with 2x SSC and then switch to a photo-protective
627 buffer containing 50% glycerol (Thermo Fisher Scientific, Waltham, MA), 75 µg/mL glucose
628 oxidase (Sigma Aldrich, Darmstadt, Germany), 520 µg/mL catalase (Sigma Aldrich,
629 Darmstadt, Germany), and 0.5 mg/mL Trolox (Sigma Aldrich, Darmstadt, Germany). Samples
630 were imaged with a spinning disk confocal microscope (OLYMPUS PlanXApo 60x/1.40- N.A.
631 oil-immersion objective, and Andor iXon camera). DAPI was excited by 405 nm, and TAMRA
632 was excited by 540 nm lasers. The distance of Z-stacks was set to 0.5 µm. The exposure time
633 and laser intensity were set to reach a maximum gray value of 16000 each image.
634
635 **Probe design of ARTseq-FISH**
636 The mRNA sequences were obtained from NCBI website (Mus musculus). Probes were
637 designed according to the targeted regions by using online software
638 (http://biosearchtech.com/stellaris-designer/), for individual probe sequences see Table S1. For
639 targeting RNA directly, we selected 36 nt from the mRNA sequence (18 nt for 5' arm and 18
640 nt for 3'arm of PLP). Each PLP contains two arms (18 nt each) for binding to the targeting
641 region, one unique 28 nt sequence identical to the bridge probe and one common RCA primer
642 binding region. Besides the 28 nt sequences identical to paired PLPs, BrPs consist of four
643 overhang sequences with 18 nt each.
644
645 Oligonucleotides used for antibody conjugation consist of a 10 nt linker (polyA) and a 36 nt
646 sequences corresponding to the complementary PLP. The 36 nt sequences for antibody
647 conjugation, 28 nt sequences of PLPs and BrPs, and 18nt readout probe sequences were
648 identified using a previously published algorithm [24]. The readout probes are 18 nt in length and
649 labeled with three different fluorophores (ATTO488, TAMRA, CY5). We used BLAST from
650 NCBI to check that the 18 nt probe sequence is less than 13 nt (<70%) complementary to other
651 Mus musculus transcripts. All the probes have GC content within the range 45%-65% and were
652 purchased from Integrated DNA technologies (IDT).
653

| | |
|---|---|
| **Oligonucleotides (46 nt)** | **5'- Azide-AAAAAAAAAA- [36 nt unique sequence] -3'** |
| **Padlock probe (84 nt)** | 5' -phosphorylated- [18 nt 5'-arm] - [28 nt unique sequence] - [20 nt RCA primer] - [18 nt 3'- arm] - 3' |
| **Bridge probe (108 nt)** | 5' - [readout 1] -AA- [readout 2] -AA- [28 nt unique sequence] -AA- [readout 3] -AA- [readout 4] - 3' |

654
655 **Antibody–DNA conjugation**
656 Antibodies (Abs) used in ARTseq-FISH were labelled with DNA oligonucleotides as previous
657 described[39]. In brief, Abs were first buffer exchanged into 0.2 M NaHCO3 (pH 8.3) (Thermo
658 Scientific Acros 217125000) by using Zeba™ Spin Desalting Columns, 40K MWCO (Thermo
659 Scientific™ 87767). Abs were then reacted with 10x molar excess of dibenzocyclooctyne-S-
660 S-N-hydroxysuccinimidyl (DBCO-S-S-NH) ester (Sigma Aldrich, 761532-1mg) for 2 hours at
661 room temperature in the dark. Next, Abs were purified using Zeba™ Spin Desalting Columns,

662 40K MWCO to remove excess DBCO-s-s-NHS. 5' Azide modified DNA oligonucleotides
663 (IDT) were incubated with Abs (molar ratio of antibody to single-stranded DNA of 1:15)
664 overnight at 4°C in the dark. The conjugated Abs were buffer exchanged into PBS (Gibco™
665 20012019) containing 0.05% sodium azide (Sigma Aldrich, S8032-25G) and 0.1 mM EDTA
666 (Lonza, 51201), and excess oligos were removed by 100K Amicon centrifuge filters (Merck
667 UFC510096). The DNA-conjugated Abs were stored at 4°C. The list of antibodies and
668 corresponding DNA oligonucleotides is provided in Table S1 and S2. The dilution of
669 conjugated antibodies was optimized between ratios of 1:1000, 1:2000 and at 1:4000 and the
670 ratio of 1:4000 was used for ARTseq-FISH.
671
672 **ARTseq-FISH**
673 ***Fixation and permeabilization*** Cells were fixed with 4% PFA (Sigma Aldrich, 1040021000-
674 1L) for 10 minutes at room temperature and then permeabilized with pre-chilled 100%
675 methanol at -20°C for 10 minutes. Cells were washed with 1x PBS three times after fixation
676 and permeabilization.
677 ***Blocking and Primary antibody incubation*** After permeabilization, cells were incubated in
678 blocking buffer (5% BSA in PBS containing 0.5% Triton) for 1 hour at room temperature. The
679 DNA oligonucleotide labelled primary antibodies were diluted to 1:4000 in blocking buffer
680 and incubated at room temperature for 2-4 hours.
681 ***RNA PLP hybridization and ligation*** Phosphorylated PLPs were hybridized to the mRNA
682 sequences directly at a final concentration of 100 nM/PLP. The reaction was performed
683 overnight at 37°C using 1x Ampligase ligase buffer (Lucigen, A1905B), 50 mM KCl
684 (Invitrogen, AM9640G), 20% Formamide (Invitrogen, AM9342), 0.2 µg/µL tRNA, 1U/ µL
685 RiboLock RNase Inhibitor (Thermo Scientific, EO0381) and 0.2 µg/µL of BSA in Nuclease-
686 free water (Invitrogen, AM9937). Next, PLP ligation was performed for 4 hours at room
687 temperature using 0.5 U/µl SplintR Ligase (NEB, M0375), 1x Ampligase ligase buffer, 10 µM
688 ATP (Invitrogen, 18330019) and 0.2 µg/µL of BSA in Nuclease-free water.
689 ***Ab PLP hybridization and ligation*** The hybridization of PLPs to DNA oligonucleotides
690 conjugated to Abs was performed at a final concentration of 5 nM/PLP. The ligation of PLPs
691 was performed in the same reaction with T4 DNA ligase, 1x T4 DNA ligase buffer, 50 mM
692 KCl (Invitrogen, AM9640G), 20% Formamide (Invitrogen, AM9342), 0.2 µg/µL of BSA and
693 Nuclease-free water. This reaction was incubated at 37°C for 30 minutes followed by 45°C for
694 90 minutes.
695 ***Rolling circle amplification (RCA)*** RCA was performed with 0.5 U/µL Phi29 polymerase
696 (NEB, M0269L), 1x Phi29 polymerase buffer, 5% Glycerol (Sigma, G5516), 0.25 mM each
697 dNTP (Thermo Scientific, R0192), 0.2 U/µL Exonuclease I (Thermo Scientific, EN0581), 0.2
698 µM RCA primer and 0.2 µg/µL of BSA in Nuclease-free water overnight at 30˚C.
699 ***Bridge probe hybridization*** BrPs were hybridized at a final concentration of 100 nM per probe.
700 The reaction took place in the hybridization buffer which contains 2x SSC, 20% formamide,
701 0.05 g/mL dextran sulfate and nuclease-free water, for 1-2 hours at room temperature. An extra
702 fixation with 4% PFA was performed to stabilize the binding of bridge probes and rolling circle
703 amplification products.
704 ***Readout probe hybridization*** RoPs were hybridized at a final concentration of 100 nM per
705 probe and in the same hybridization buffer as the BrPs. The reaction can be performed together
706 with DAPI (10 µg/mL) (Thermo Scientific™ 62247) staining for 1h at room temperature. Cells
707 were washed with 2x SSC and then switch to a photo-protective buffer containing 50% glycerol
708 (Thermo Fisher Scientific, Waltham, MA), 75 µg/mL glucose oxidase (Sigma Aldrich,
709 Darmstadt, Germany), 520 µg/mL catalase (Sigma Aldrich, Darmstadt, Germany), and 0.5
710 mg/mL Trolox (Sigma Aldrich, Darmstadt, Germany).

711 ***Image acquisition*** Images of sequential hybridization were acquired with a spinning disk
712 confocal microscope (OLYMPUS PlanXApo 60x/1.40- N.A. oil-immersion objective, and
713 Andor iXon camera). DAPI was excited by 405 nm, and ATTO488, TAMRA, Cy5 was excited
714 by 475 nm, 540 nm and 638 nm lasers respectively. The distance of Z-stacks was set as 0.5 µm.
715 The exposure time and laser intensity were set differently in different channels to obtain the
716 same maximum intensity value of spots.
717 ***Stripping*** Samples were incubated in 60% formamide solution (60% formamide in 2x SSC)
718 for 10 mins to remove the readout probes after image acquisition and then washed three times
719 with 2x SSC.
720 ***Rehybridization*** A new set of RoPs were hybridized in the hybridization buffer for 1hour at
721 room temperature in dark.
722 ***Image acquisition*** Same as described above. Repeat the cycle of image acquisition, stripping
723 off readout probes and rehybridization.
724
725 **Single-cell RNA sequencing (scRNAseq) in mESCs**
726 mESC were cultured as previous described. Cells were grown for 30 hours in a 37 °C incubator
727 with 5% $CO_2$. Cells were exposed to 0.007% EtOH for the last 6 hours. Cells were then washed
728 once with PBS and detached by 0.05% trypsin-EDTA for 2 minutes at 37 °C. Detached cells
729 were pelleted and resuspended in 1mL of freezing media consisting of 80% culture media, 10%
730 of extra heat inactivated FBS and 10% of DMSO. Proper viability of the cells prior to freezing
731 was quantified with propidium iodide/acridine orange staining in a LUNA-FL Dual
732 Fluorescence Cell Counter. Frozen cells were delivered to the commercial company Single
733 Cell Discoveries (https://www.scdiscoveries.com) in dry ice. Single cell barcoding was
734 performed in a 10x microfluidic genomic chip in order to encapsulate individual cells in water
735 droplets in oil, containing cell specific barcoded beads. Labelled RNA molecules were pooled
736 and subjected to a poly-A specific reverse transcription. cDNA molecules where linearly
737 amplified using an in vitro transcription reaction and the final sequencing library was obtained
738 through a second step of reverse transcription. 3'-end sequencing was performed, followed by
739 quality control and genomic mapping. Final read count per gene and per cell matrices where
740 generated and used in posterior analysis steps.
741
742 **Flow cytometry analysis of cell cycle**
743 mESCs were seeded in 1.9 $cm^2$ wells (24-well format) with a density of 4.4 x $10^3$ cells/$cm^2$.
744 The wells were previously coated with 0.1% gelatin. Cells were seeded in serum/LIF medium
745 and cultured for 24 hours. Then, cells were fixed in pre-chilled 70% ethanol for 30 minutes at
746 -20°C and washed by 1x PBS. Finally, cells were stained with 1 µg/mL propidium iodide
747 (Sigma-Aldrich, P4864-10ML) containing 10 µg/mL RNaseA (VWR International B.V, 0675-
748 250MG) for 15 minutes. After staining, cells were transferred to a flow cytometry tube and
749 kept on ice until their immediate analysis in a BD FACS Calibur™ flow cytometer.
750
751 **Flow cytometry analysis of NANOG-GFP mESC cell line in serum/LIF conditions**
752 The NANOG-GFP mESC line was kindly provided by Leor Weinberger's lab (Gladstone
753 Institutes)[58]. NANOG-GFP mESCs and non-labelled mESCs were seeded in 9.5 $cm^2$ wells (6-
754 well format) with a density of 4x $10^4$ cells/$cm^2$. The wells were previously coated with 0.1%
755 gelatin. Cells were seeded in serum/LIF medium. 24 hours post-seeding, cells were detached
756 with 400 µL of 0.05% trypsin-EDTA for 2 minutes and resuspended in growing media. Cells
757 were transferred to a flow cytometry tube and kept on ice until their immediate analysis in a
758 BD FACS Calibur™ flow cytometer.
759
760 **Flow cytometry analysis of CD24 expression in mESC**

761 mESCs were seeded in 1.9 $cm^2$ wells (24-well format) with a density of 4.4x $10^3$ cells/$cm^2$.
762 The wells were previously coated with 0.1% gelatin. Cells were seeded in serum/LIF medium
763 and cultured for 96 hours, with a medium renewal at 48 hours of culture. Cells were stained
764 with an anti-mouse CD24 antibody conjugated to alexa647 fluorophore (BioLegend, 101818)
765 or an alexa647 isotype control antibody (BioLegend, 400626) for 30 minutes in serum/LIF
766 media at 37˚C. After staining, cells were washed with 1x PBS and detached with accutase
767 (StemCell™ technologies, 07922) for 5 minutes at 37˚C, transferred to a flow cytometry tube
768 and kept on ice until their analysis in a BD FACSVerse™ flow cytometer.
769
770 **EdU proliferation assay**
771 mESCs were seeded onto the micropatterns, ensuring complete coverage, and cultured for 16
772 hours. Subsequently, the medium was changed to a LIF-free medium. To assess cell
773 proliferation at different time points, the culture medium was supplemented with 10 µM of
774 EdU two hours before fixation at each time point. The detection of EdU incorporation was
775 performed according to the protocol provided by the EdU proliferation kit (Abcam, ab219801,
776 iFluor 488). In brief, the cells were washed twice with Wash Buffer and then fixed with 4%
777 PFA for 10 minutes at room temperature, while avoiding exposure to light. After the fixation
778 step, the cells were washed twice and permeabilized with 1x Permeabilization Buffer for 20
779 minutes at room temperature. Subsequently, the cells were washed twice and incubated in the
780 dark for 30 minutes at room temperature in a Reaction mix containing TBS, 4 mM Copper
781 Sulfate, 1.2 µM iFluor 488 azide dye (500 µM in DMSO), and 1x EdU additive solution.
782 Following another round of washing, the cells were stained with Hoechst 33342 (5 µg/mL).
783 Finally, the cells were imaged using a spinning disk confocal microscope (OLYMPUS
784 UPlanFL N 10x/0.30 N.A. objective, and Andor iXon camera). The Hoechst 33342 and EdU
785 signals were excited at wavelengths of 405 nm and 475 nm, respectively.
786
787 **Protein synthesis assay**
788 mESCs were seeded onto the micropatterns, ensuring complete coverage, and cultured for 16
789 hours. Subsequently, the medium was changed to a LIF-free medium. To assess the protein
790 synthesis at different time points, the culture medium was supplemented with 20 µM of Click-
791 iT® OPP 30 minutes before fixation at each time point. The detection of protein synthesis was
792 performed according to the protocol provided by the Click-iT® Plus OPP Protein Synthesis
793 Assay Kits (Thermo Fisher, C10456). In brief, the cells were washed once with 1x PBS and
794 then fixed with 4% PFA for 10 minutes at room temperature. After the fixation step, the cells
795 were washed twice and permeabilized with 0.5% Triton-X-100 in PBS for 15 minutes at room
796 temperature. Subsequently, the cells were washed twice and incubated in the dark for 30
797 minutes at room temperature in a Click-iT® Plus OPP reaction cocktail containing 1x Click-
798 iT® OPP Reaction Buffer, Copper Protectant (Component D), Alexa Fluor® picolyl azide
799 (Component B) and 1x Click-iT® Reaction Buffer Additive. Following another round of
800 washing, the cells were stained with 1X HCS NuclearMask™ Blue Stain for 30 minutes at
801 room temperature, protected from light. Finally, the cells were imaged using a spinning disk
802 confocal microscope (OLYMPUS UPlanFL N 10x/0.30 N.A. objective, and Andor iXon
803 camera). The NuclearMask™ Blue Stain and protein synthesis signals were excited at
804 wavelengths of 405 nm and 638 nm, respectively.
805
806 **Apoptosis detection**
807 To detect apoptosis of mESCs, Cleaved Caspase-3 (Cell Signaling, 94530) and 7-AAD
808 (Thermier Fisher, 00-6993-50) were measured to assess the middle and late stage of apoptosis
809 respectively. mESCs were seeded onto the micropatterns, ensuring complete coverage, and
810 cultured for 16 hours. Subsequently, the medium was changed to a LIF-free medium. To assess

811 the middle stage of apoptosis after 48 hours differentiation, fixed cells were stained with
812 Caspase-3 (cleaved) as mentioned in the section of " Immunostaining". To assess the late stage
813 of apoptosis after 48 hours differentiation, live cells were stained with 7-AAD and Hoechst
814 33342 (Sigma-Aldrich, B2261-25MG) for 30 minutes at a 37°C incubator. Finally, the cells
815 were imaged using a spinning disk confocal microscope (OLYMPUS UPlanFL N 10x/0.30
816 N.A. objective, and Andor iXon camera). Quantification of apoptosis from nuclear morphology
817 was performed on DAPI images acquired by ART-seqFISH as previously described[63].
818
819 **Live cell imaging**
820 Fucci mESCs[65, 66] were kindly provided by Menno Ter Huurne and Hendrik Marks at Radboud
821 University. NANOG-GFP mESCs[58, 59] and Fucci mESCs were seeded onto the micropatterns,
822 ensuring complete coverage, and cultured for 16 hours. Subsequently, the medium was changed
823 to a LIF-free medium and live cell imaging was performed after LIF withdrawal. Imaging was
824 conducted using the SP8x AOBS-WLL confocal laser scanning microscope, equipped with a
825 Leica 40x/1.1 Water objective and a live-cell environmental chamber maintained at a
826 humidified temperature of 37°C and 5% $CO_2$. For NANOG-GFP mESCs, images were
827 acquired using a HyDs detector and a 488 nm laser. As for Fucci mESCs, images were acquired
828 using a HyDs detector, along with both 488 nm and 561 nm lasers. Z-series was obtained with
829 a step size of 1.5 µm. The time interval between image acquisitions was set to 1.5 hours. Single
830 cell tracking was performed manually using the Multi-point tool in Fiji[85].
831
832 **Image and data analysis**
833 Details described in Supplementary Information, Supplementary Note 2: Computational
834 pipelines development of ARTseq-FISH.
835
836 **Data availability**
837 All data is available in the main text or the supplementary information.

838 **References**


839 1. Rivron, N.C. et al. Blastocyst-like structures generated solely from stem cells. *Nature*
840 **557**, 106-111 (2018).
841 2. Martyn, I., Kanno, T.Y., Ruzo, A., Siggia, E.D. & Brivanlou, A.H. Self-organization
842 of a human organizer by combined Wnt and Nodal signalling. *Nature* **558**, 132-135
843 (2018).
844 3. Girgin, M.U. et al. Bioengineered embryoids mimic post-implantation development in
845 vitro. *Nat Commun* **12**, 5140 (2021).
846 4. Lolas, M., Valenzuela, P.D.T., Tjian, R. & Liu, Z. Charting Brachyury-mediated
847 developmental pathways during early mouse embryogenesis. *Proceedings of the*
848 *National Academy of Sciences* **111**, 4478-4483 (2014).
849 5. Li, Z. et al. BMP4 Signaling Acts via Dual-Specificity Phosphatase 9 to Control ERK
850 Activity in Mouse Embryonic Stem Cells. *Cell Stem Cell* **10**, 171-182 (2012).
851 6. Pauklin, S. & Vallier, L. The Cell-Cycle State of Stem Cells Determines Cell Fate
852 Propensity. *Cell* **155**, 135-147 (2013).
853 7. Lu, R. et al. Systems-level dynamic analyses of fate change in murine embryonic stem
854 cells. *Nature* **462**, 358-362 (2009).
855 8. Abranches, E. et al. Stochastic NANOG fluctuations allow mouse embryonic stem
856 cells to explore pluripotency. *Development* **141**, 2770-2779 (2014).
857 9. Hu, S. et al. Transcription factor antagonism regulates heterogeneity in embryonic
858 stem cell states. *Mol Cell* **82**, 4410-4427.e4412 (2022).
859 10. Martyn, I., Brivanlou, A.H. & Siggia, E.D. A wave of WNT signaling balanced by
860 secreted inhibitors controls primitive streak formation in micropattern colonies of
861 human embryonic stem cells. *Development* **146** (2019).
862 11. Etoc, F. et al. A Balance between Secreted Inhibitors and Edge Sensing Controls
863 Gastruloid Self-Organization. *Developmental Cell* **39**, 302-315 (2016).
864 12. Morgani, S.M., Metzger, J.J., Nichols, J., Siggia, E.D. & Hadjantonakis, A.K.
865 Micropattern differentiation of mouse pluripotent stem cells recapitulates embryo
866 regionalized cell fate patterning. *Elife* **7** (2018).
867 13. Chhabra, S., Liu, L., Goh, R., Kong, X. & Warmflash, A. Dissecting the dynamics of
868 signaling events in the BMP, WNT, and NODAL cascade during self-organized fate
869 patterning in human gastruloids. *PLoS Biol* **17**, e3000498 (2019).
870 14. Tewary, M. et al. A stepwise model of reaction-diffusion and positional information
871 governs self-organized human peri-gastrulation-like patterning. *Development* **144**,
872 4298-4312 (2017).
873 15. Minn, K.T. et al. High-resolution transcriptional and morphogenetic profiling of cells
874 from micropatterned human ESC gastruloid cultures. *Elife* **9**, e59445 (2020).
875 16. Blin, G. et al. Geometrical confinement controls the asymmetric patterning of
876 brachyury in cultures of pluripotent cells. *Development* **145** (2018).
877 17. Plouhinec, J.-L., Simon, G., Vieira, M., Collignon, J. & Sorre, B. Dissecting signaling
878 hierarchies in the patterning of the mouse primitive streak using micropatterned
879 EpiLC colonies. *Stem Cell Rep* **17**, 1757-1771 (2022).
880 18. Merritt, C.R. et al. Multiplex digital spatial profiling of proteins and RNA in fixed
881 tissue. *Nat Biotechnol* **38**, 586-599 (2020).
882 19. Vickovic, S. et al. High-definition spatial transcriptomics for in situ tissue profiling.
883 *Nat Methods* **16**, 987-990 (2019).
884 20. Liu, Y. et al. High-Spatial-Resolution Multi-Omics Sequencing via Deterministic
885 Barcoding in Tissue. *Cell* **183**, 1665-1681 e1618 (2020).
886 21. Stahl, P.L. et al. Visualization and analysis of gene expression in tissue sections by
887 spatial transcriptomics. *Science* **353**, 78-82 (2016).

888 22. Chen, A. et al. Spatiotemporal transcriptomic atlas of mouse organogenesis using
889 DNA nanoball-patterned arrays. *Cell* **185**, 1777-1792.e1721 (2022).
890 23. Codeluppi, S. et al. Spatial organization of the somatosensory cortex revealed by
891 osmFISH. *Nature Methods* **15**, 932-935 (2018).
892 24. Moffitt, J.R. et al. High-throughput single-cell gene-expression profiling with
893 multiplexed error-robust fluorescence in situ hybridization. *Proc Natl Acad Sci U S A*
894 **113**, 11046-11051 (2016).
895 25. Chen, K.H., Boettiger, A.N., Moffitt, J.R., Wang, S. & Zhuang, X. Spatially resolved,
896 highly multiplexed RNA profiling in single cells. *Science* **348**, aaa6090 (2015).
897 26. Takei, Y. et al. Integrated spatial genomics reveals global architecture of single
898 nuclei. *Nature* **590**, 344-350 (2021).
899 27. Eng, C.-H.L. et al. Transcriptome-scale super-resolved imaging in tissues by RNA
900 seqFISH+. *Nature* **568**, 235-239 (2019).
901 28. Wang, G., Moffitt, J.R. & Zhuang, X. Multiplexed imaging of high-density libraries
902 of RNAs with MERFISH and expansion microscopy. *Sci Rep-Uk* **8**, 4847 (2018).
903 29. Rao, A., Barkley, D., Franca, G.S. & Yanai, I. Exploring tissue architecture using
904 spatial transcriptomics. *Nature* **596**, 211-220 (2021).
905 30. Wang, F. et al. RNAscope: a novel in situ RNA analysis platform for formalin-fixed,
906 paraffin-embedded tissues. *J Mol Diagn* **14**, 22-29 (2012).
907 31. Popovic, D., Koch, B., Kueblbeck, M., Ellenberg, J. & Pelkmans, L. Multivariate
908 Control of Transcript to Protein Variability in Single Mammalian Cells. *Cell Syst* **7**,
909 398-411 e396 (2018).
910 32. Schulz, D. et al. Simultaneous Multiplexed Imaging of mRNA and Proteins with
911 Subcellular Resolution in Breast Cancer Tissue Samples by Mass Cytometry. *Cell*
912 *Syst* **6**, 25-36 e25 (2018).
913 33. Goltsev, Y. et al. Deep Profiling of Mouse Splenic Architecture with CODEX
914 Multiplexed Imaging. *Cell* **174**, 968-981 e915 (2018).
915 34. Saka, S.K. et al. Immuno-SABER enables highly multiplexed and amplified protein
916 imaging in tissues. *Nat Biotechnol* **37**, 1080-1090 (2019).
917 35. Manesse, M., Patel, K.K., Bobrow, M. & Downing, S.R. in Biomarkers for
918 Immunotherapy of Cancer: Methods and Protocols. (eds. M. Thurin, A. Cesano &
919 F.M. Marincola) 585-592 (Springer New York, New York, NY; 2020).
920 36. He, S. et al. High-plex imaging of RNA and proteins at subcellular resolution in fixed
921 tissue by spatial molecular imaging. *Nature Biotechnology* (2022).
922 37. Vistain, L. et al. Quantification of extracellular proteins, protein complexes and
923 mRNAs in single cells by proximity sequencing. *Nature Methods* **19**, 1578-1589
924 (2022).
925 38. van Buggenum, J.A.G. et al. Immuno-detection by sequencing enables large-scale
926 high-dimensional phenotyping in cells. *Nat Commun* **9**, 2384 (2018).
927 39. Rivello, F. et al. Single-cell intracellular epitope and transcript detection reveals
928 signal transduction dynamics. *Cell Reports Methods* **1**, 100070 (2021).
929 40. Sountoulidis, A. et al. SCRINSHOT enables spatial mapping of cell states in tissue
930 sections with single-cell resolution. *PLoS Biol* **18**, e3000675 (2020).
931 41. Lee, H., Marco Salas, S., Gyllborg, D. & Nilsson, M. Direct RNA targeted in situ
932 sequencing for transcriptomic profiling in tissue. *Sci Rep* **12**, 7976 (2022).
933 42. Alon, S. et al. Expansion sequencing: Spatially precise in situ transcriptomics in intact
934 biological systems. *Science* **371** (2021).
935 43. Gyllborg, D. et al. Hybridization-based in situ sequencing (HybISS) for spatially
936 resolved transcriptomics in human and mouse brain tissue. *Nucleic Acids Res* **48**, e112
937 (2020).

44. Collaboration, T.A. et al. Astropy: A community Python package for astronomy. *A&A* **558**, A33 (2013).
45. Zhou, Q.-Y., Park, J. & Koltun, V. Open3D: A modern library for 3D data processing. *arXiv preprint arXiv:1801.09847* (2018).
46. Bradski, G. The openCV library. *Dr. Dobb's Journal: Software Tools for the Professional Programmer* **25**, 120-123 (2000).
47. Waskom, M.L. Seaborn: statistical data visualization. *Journal of Open Source Software* **6**, 3021 (2021).
48. McKinney, W. in Proceedings of the 9th Python in Science Conference, Vol. 445 51-56 (Austin, TX, 2010).
49. Pedregosa, F. et al. Scikit-learn: Machine learning in Python. *the Journal of machine Learning research* **12**, 2825-2830 (2011).
50. Hansen, M.M.K., Desai, R.V., Simpson, M.L. & Weinberger, L.S. Cytoplasmic Amplification of Transcriptional Noise Generates Substantial Cell-to-Cell Variability. *Cell Syst.* **7**, 384-397.e386 (2018).
51. van Sluijs, B., Maas, R.J.M., van der Linden, A.J., de Greef, T.F.A. & Huck, W.T.S. A microfluidic optimal experimental design platform for forward design of cell-free genetic networks. *Nature Communications* **13**, 3626 (2022).
52. Acampora, D. et al. Functional Antagonism between OTX2 and NANOG Specifies a Spectrum of Heterogeneous Identities in Embryonic Stem Cells. *Stem Cell Reports* **9**, 1642-1659 (2017).
53. Guo, G. et al. Serum-Based Culture Conditions Provoke Gene Expression Variability in Mouse Embryonic Stem Cells as Revealed by Single-Cell Analysis. *Cell Rep* **14**, 956-965 (2016).
54. Marks, H. et al. The Transcriptional and Epigenomic Foundations of Ground State Pluripotency. *Cell* **149**, 590-604 (2012).
55. Hao, Y. et al. Integrated analysis of multimodal single-cell data. *Cell* **184**, 3573-3587.e3529 (2021).
56. Raj, A., Peskin, C.S., Tranchina, D., Vargas, D.Y. & Tyagi, S. Stochastic mRNA Synthesis in Mammalian Cells. *PLOS Biology* **4**, e309 (2006).
57. Semrau, S. et al. Dynamics of lineage commitment revealed by single-cell transcriptomics of differentiating embryonic stem cells. *Nature Communications* **8**, 1096 (2017).
58. Desai, R.V. et al. A DNA repair pathway can regulate transcriptional noise to promote cell fate transitions. *Science* **373**, eabc6506 (2021).
59. Sokolik, C. et al. Transcription Factor Competition Allows Embryonic Stem Cells to Distinguish Authentic Signals from Noise. *Cell Syst* **1**, 117-129 (2015).
60. Altman, M.K. et al. Suppression of the GTPase-activating protein RGS10 increases Rheb-GTP and mTOR signaling in ovarian cancer cells. *Cancer Lett* **369**, 175-183 (2015).
61. Salic, A. & Mitchison, T.J. A chemical method for fast and sensitive detection of DNA synthesis in vivo. *Proceedings of the National Academy of Sciences* **105**, 2415-2420 (2008).
62. Cai, C. et al. c-Myc regulates neural stem cell quiescence and activation by coordinating the cell cycle and mitochondrial remodeling. *Signal Transduction and Targeted Therapy* **6**, 306 (2021).
63. Filippi-Chiela, E.C. et al. Nuclear Morphometric Analysis (NMA): Screening of Senescence, Apoptosis and Nuclear Irregularities. *PLOS ONE* **7**, e42522 (2012).
64. Miller, I. et al. Ki-67 is a Graded Rather than a Binary Marker of Proliferation versus Quiescence. *Cell Rep* **24**, 1105-1112.e1105 (2018).

65. Ter Huurne, M., Chappell, J., Dalton, S. & Stunnenberg, H.G. Distinct Cell-Cycle Control in Two Different States of Mouse Pluripotency. *Cell Stem Cell* **21**, 449-455.e444 (2017).
66. ter Huurne, M. et al. Critical Role for P53 in Regulating the Cell Cycle of Ground State Embryonic Stem Cells. *Stem Cell Rep* **14**, 175-183 (2020).
67. Ferro, A. et al. Blue intensity matters for cell cycle profiling in fluorescence DAPI-stained images. *Laboratory Investigation* **97**, 615-625 (2017).
68. Olofsson, K., Carannante, V., Takai, M., Önfelt, B. & Wiklund, M. Single cell organization and cell cycle characterization of DNA stained multicellular tumor spheroids. *Sci Rep-Uk* **11**, 17076 (2021).
69. Roukos, V., Pegoraro, G., Voss, T.C. & Misteli, T. Cell cycle staging of individual cells by fluorescence microscopy. *Nat Protoc* **10**, 334-348 (2015).
70. Tao, Y. et al. Highly efficient and robust π-FISH rainbow for multiplexed in situ detection of diverse biomolecules. *Nature Communications* **14**, 443 (2023).
71. Palla, G., Fischer, D.S., Regev, A. & Theis, F.J. Spatial components of molecular tissue biology. *Nature Biotechnology* **40**, 308-318 (2022).
72. Stuart, T. & Satija, R. Integrative single-cell analysis. *Nature Reviews Genetics* **20**, 257-272 (2019).
73. Qin, Y. et al. A multi-scale map of cell structure fusing protein images and interactions. *Nature* **600**, 536-542 (2021).
74. Szemes, M. et al. Diagnostic application of padlock probes--multiplex detection of plant pathogens using universal microarrays. *Nucleic Acids Res* **33**, e70 (2005).
75. Fang, C. et al. MiRNA Detection Using a Rolling Circle Amplification and RNA-Cutting Allosteric Deoxyribozyme Dual Signal Amplification Strategy. *Biosensors (Basel)* **11** (2021).
76. Lin, C. et al. Visualization of individual microRNA molecules in fixed cells and tissues using target-primed padlock probe assay. *Biochemical and Biophysical Research Communications* **526**, 607-611 (2020).
77. Kumari, R. et al. A Novel Rolling Circle Amplification-Based Detection of SARS-CoV-2 with Multi-Region Padlock Hybridization. *Diagnostics* **12** (2022).
78. Söderberg, O. et al. Direct observation of individual endogenous protein complexes in situ by proximity ligation. *Nature Methods* **3**, 995-1000 (2006).
79. Jain, S., Dandy, D.S., Geiss, B.J. & Henry, C.S. Padlock probe-based rolling circle amplification lateral flow assay for point-of-need nucleic acid detection. *Analyst* **146**, 4340-4347 (2021).
80. Zhao, Y. et al. Single Cell RNA Expression Analysis Using Flow Cytometry Based on Specific Probe Ligation and Rolling Circle Amplification. *Acs Sensors* **5**, 3031-3036 (2020).
81. van Mierlo, G. et al. Integrative Proteomic Profiling Reveals PRC2-Dependent Epigenetic Crosstalk Maintains Ground-State Pluripotency. *Cell Stem Cell* **24**, 123-137.e128 (2019).
82. Théry, M. & Piel, M. Adhesive micropatterns for cells: a microcontact printing protocol. *Cold Spring Harb Protoc* **2009**, pdb.prot5255 (2009).
83. van Kooten, T.G., Spijker, H.T. & Busscher, H.J. Plasma-treated polystyrene surfaces: model surfaces for studying cell-biomaterial interactions. *Biomaterials* **25**, 1735-1747 (2004).
84. Bao, M., Xie, J., Piruska, A. & Huck, W.T.S. 3D microniches reveal the importance of cell size and shape. *Nat Commun* **8**, 1962 (2017).
85. Schindelin, J. et al. Fiji: an open-source platform for biological-image analysis. *Nature Methods* **9**, 676-682 (2012).

**Acknowledgments**

We thank members of the Huck and Hansen laboratories for the thoughtful discussion and suggestions; Aigars Piruska for making the silicon masters with micropatterns and technical assistance with CSU spinning disk confocal; Erik van Buijtenen and Kinga Matuła for sharing the antibody conjugation protocols, and fruitful discussions and suggestions from Erik van Buijtenen. We also thank Leor Weinberger for the NANOG-GFP mESC line as well as Hendrik Marks for the mESC-E14 and mESC Fucci cell line and thoughtful suggestions. We acknowledge generous support from Radboud University (W.T.S.H.), the Christine Mohrmann fellowship (M.M.K.H), the European Union (ERC, ChOICE, 101041939, M.M.K.H) and the Netherlands Organization for Scientific Research (NWO) (ENW-XS awards OCENW.XS3.055 and OCENW.XS21.2.050, both M.M.K.H., and a Spinoza grant, W.T.S.H.). X.H. acknowledges financial support from the China Scholarship Council (CSC).

**Author information**

Authors and Affiliations

**Institute for Molecules and Materials, Radboud University, Heyendaalseweg 135, 6525 AJ Nijmegen, the Netherlands**

Xinyu Hu, Bob van Sluijs, Óscar García-Blay, Yury Stepanov, Koen Rietrae, Wilhelm T.S. Huck, Maike M. K. Hansen.

Contributions

X.H., B.v.S., W.T.S.H., and M.M.K.H. conceived and designed the study. X.H. developed and optimized the experimental procedure for ARTseq-FISH. B.v.S. developed the software for ARTseq-FISH. Ó.G.B. helped with probe design and optimization of ARTseq-FISH workflow. Ó.G.B., also conducted supporting experiments. Y.S., and K.R., contributed to validation experiments of ARTseq-FISH. X.H., B.v.S., W.T.S.H., and M.M.K.H. wrote the manuscript and Ó.G.B. edited the manuscript.

Corresponding author

Correspondence to Wilhelm T.S. Huck and Maike M. K. Hansen.

**Ethics declarations**

Competing interests

Authors declare no competing interests

**Supplementary Information:**

Supplementary Notes 1 Experimental development of ARTseq-FISH

Supplementary Notes 2 Computational pipeline development of ARTseq-FISH

Supplementary Figs. 1-31

Supplementary Table Captions

References

**Supplementary Tables 1-5**